1

2

3

4 **New particle formation in the Svalbard region 2006 - 2015**

5

6 Jost Heintzenberg[1], Peter Tunved[2], Martí Galí[3], and Caroline Leck[4]

7

8

9 1: Leibniz Institute for Tropospheric Research (TROPOS), Permoserstr. 15, 04318 Leipzig,

10 Germany

11 2: Department of Environmental Science and Analytical Chemistry (ACES), Stockholm

12 University, 10691 Stockholm, Sweden

13 3: Takuvik Joint International Laboratory & Québec-Océan, Université Laval, G1V 0A6

14 Québec, Canada

15 4: Department of Meteorology, Stockholm University (MISU), 10691 Stockholm, Sweden

16

17   Abstract

18

19   Events of new particle formation, (NPF), were analyzed in a ten-year data set of hourly

20   particle size distributions recorded on Mt. Zeppelin, Spitsbergen, Svalbard. Three different

21   types of NPF-events were identified through objective search algorithms. The first and

22   simplest algorithm utilizes short-term increases in particle concentrations below 25 nm,

23   (PCT-events). The second one builds on the growth of the sub-50 nm diameter-median,

24   (DGR-events), and is most closely related to the classical "banana-type" of events. The third

25   and most complex, so-called multiple-size approach to identifying NPF-events builds on a

26   hypothesis suggesting the concurrent production of polymer gel particles at several sizes

27   below about 60 nm, (MEV-events).

28   As a first and general conclusion we can state that NPF-events are a summer phenomenon

29   and not related to Arctic haze, which is a late winter-to-early spring feature. The occurrence

30   of NPF-events appears to be somewhat sensitive to the available data on precipitation. The

31   seasonal distribution of solar flux suggests some photochemical control that may affect

32   marine biological processes generating particle precursors and/or atmospheric photochemical

33   processes that generate condensable vapors from precursor gases. Notable, the seasonal

34   distribution of the biogenic methanesulfonate, (MSA), follows that of the solar flux although

35   it peaks before the maxima in NPF-occurrence.

36   A host of ancillary data and findings point to varying and rather complex marine biological

37   source processes. The potential source regions for all types of new particle formation appear

38   to be restricted to the marginal ice and open water areas between Northeastern Greenland and

39   Eastern Svalbard. Depending on conditions yet to be clarified new particle formation may

40   become visible as short bursts of particles around 20 nm, (PCT-events), longer events

41   involving condensation growth, (DGR-events), or extended events with elevated

42   concentrations of particles at several sizes below 100 nm, (MEV-events). The seasonal

43   distribution of NPF-events peaks later than that of MSA and, DGR and in particular of MEV-

44   events reach into late summer and early fall with much open, warm, and biologically active

45   waters around Svalbard. Consequently, a simple model to describe the seasonal distribution

46   of the total number of NPF-events can be based on solar flux, and sea surface temperature,

47   representing environmental conditions for marine biological activity, and condensation sink,

48   controlling the balance between new particle nucleation and their condensational growth.

49   Based on the sparse knowledge about the seasonal cycle of gel-forming marine

50   microorganisms and their controlling factors we hypothesize that the seasonal distribution of

51   DGR and more so MEV-events reflect the seasonal cycle of the gel-forming phytoplankton.

52

53

1. Introduction

In the late 1970ies and early 1980ies the interest in the Arctic atmospheric aerosol widened from the well-identified winter phenomenon of Arctic haze (Rahn and Shaw, 1977; Heintzenberg and Leck, 1994) to summer conditions in this northernmost remote region. In the pristine Arctic summer air the so-called background aerosol (Junge, 1963) was expected to be most clearly visible, far away from the northern hemispheric anthropogenic emission centers at lower latitudes. Episodic and localized occurrences of high concentrations of ultrafine particles, (here defined as particles with diameters < 100 nm), in the summer Arctic were explained by rare import of polluted air from lower latitudes (Flyger and Heidam, 1978; Heintzenberg and Larssen, 1983) or hypothetical anthropogenic sources in the Arctic (Jaenicke and Schütz, 1982).

With the advent of sensitive condensation nuclei counters (Agarwal and Sem, 1980) and differential mobility analyzers (Knutson and Whitby, 1975b, a) more details became visible in the Arctic sub-micrometer aerosol. High numbers of ultrafine particles were observed in connection with fog passages (Lannefors et al., 1983) and chemical aerosol information indicated a regional – possibly biogenic – particle sources in the summer Arctic (Heintzenberg, 1989). The high molar ratios of methane sulfonate, (MSA), to non-sea salt sulfate, ($nssSO_4^{2-}$), of 0.28 in the Arctic summer aerosol found by Heintzenberg and Leck (1994) substantiated the biogenic source of the particles.

The establishment of long-term Arctic aerosol monitoring at the fringes of the pack ice in Alaska (e.g., Polissar et al., 1999), Canada (e.g., Norman et al., 1999; Willis et al., 2016), and on Spitsbergen (e.g., Tunved et al., 2013) revealed more details of potential sources of the summer aerosol, in particular their connection to the marine biosphere in the Arctic. The unique series of systematic aerosol studies in the central Arctic north of 80°N onboard the Swedish icebreaker *Oden* in 1996 led to the formulation of a new hypothesis concerning a

80   specific process of marine biogenic particle formation (Leck and Bigg, 1999). The marine

81   biogenic particles involved behaved as polymer gels and originated in the surface microlayer

82   (SML) of the ocean, (Orellana et al., 2011b), from the activity of sea-ice algae,

83   phytoplankton and, perhaps, bacteria. The new particle events were reported to occur as

84   simultaneous enhancement of particle number concentrations in the whole size-range below

85   50 nm, and not with the prototypical "banana growth" (Kulmala et al., 2004). Two more

86   *Oden* cruises in 2001 and 2008 yielded results that were partly contradicting (Held et al.,

87   2011b; Held et al., 2011a), partly supporting the SML hypothesis (Leck et al., 2013; Karl et

88   al., 2013; Orellana et al., 2011b; Leck and Bigg, 2010). The synopsis of the results of four

89   *Oden* cruises of Heintzenberg et al. (2015) identified geographic regions of new particle

90   formation (NPF) in the inner Arctic while stressing the importance of recent open water and

91   related biological activity in the sea in transects by air masses with new particle formation

92   over the central Arctic.

93   Two years of aerosol size distributions from Mt. Zeppelin, Spitsbergen and Alert, both

94   located at the fringes of the central pack ice, were analyzed by Croft et al. (2016a) with a

95   global aerosol geophysics model. They discuss classical new-particle nucleation, coagulation

96   scavenging in clouds, scavenging by precipitation, and transport in order to explain the annual

97   cycle of the Arctic aerosol. Croft et al. (2016a) find two seasonal maxima in their modeled

98   particle nucleation rates, one in March, and one in July. In spring, their simulated NPF occurs

99   mainly in the free troposphere, whereas in summer, it occurs also in the planetary boundary

100   layer. More recently, Croft et al. (2016b) state that ammonia from seabird-colony guano is a

101   key factor contributing to bursts of newly formed particles, which are observed every summer

102   in the near-surface atmosphere, at least at Alert, Nunavut, Canada. Earlier, the results of

103   studies with another global aerosol model by Browse et al. (2014) suggested that the potential

104   increase in NPF in the Arctic with potential increases in cloud condensation nuclei is

105 compensated by wet scavenging. They also state that scavenging by pre-existing large

106 particles suppresses NPF-events.

107   Based on three years of data from the two Arctic sites Thule and Ny-Ålesund (gruvebadet)

108 Becagli et al. (2016) examined the sources and environmental factors controlling the

109 biological aerosol component MSA. Their analysis included satellite-derived Chlorophyll-*a*

110 (an indicator of phytoplankton biomass), oceanic phytoplankton primary productivity, (PPP),

111 and sea ice. Whereas they found good correlations between MSA, PPP and sea ice, (the latter

112 two being closely related), their data did not allow any statements on NPF processes.

113   To date the longest record of sub-micrometer number-size distributions of the Arctic

114 aerosol down to 5 nm particle diameter and below has been accumulated on Mt. Zeppelin,

115 Spitsbergen (Tunved et al., 2013; Heintzenberg and Leck, 1994). For the ten years from 2006

116 through 2015 a total of 63936 quality-controlled hours of aerosol data are available, i.e.

117 during 73% of all hours of the ten years. In the present study we exploit this formidable data

118 set in a search for processes forming new particles. An important first step in this work was

119 formulating completely objective criteria for the identification of events. In the relatively

120 clean Arctic environment we do not expect the classical nucleation and growth events as

121 frequently observed over the continents, (cf. Kulmala et al., 2004), to dominate. Thus, we

122 refrained from applying the objective search algorithm formulated by Heintzenberg et al.,

123 (2007) for this "Banana-type" of events. Instead we formulated new objective search

124 algorithms allowing several potential types of new particle formation events or formation

125 processes. With a host of complementary atmospheric and surface physical, chemical, and

126 biological information a large number of NPF-events identified with these algorithms will be

127 analyzed in the following chapters.

128

129

130

2. Database

The Mt. Zeppelin observatory

Situated at the top of Mt Zeppelin, Svalbard (78° 56'N, 11° 53'E), the Zeppelin observatory offers a unique possibility to study the characteristic features of Arctic atmospheric constituents such as trace gases and aerosol particles. At a height of 474 m a.s.l. the station is located near the top of the local planetary boundary layer and represents remote Arctic conditions. The closest source of pollution, the small community of Ny-Ålesund, is located ~2 km north of the station (http://www.esrl.noaa.gov/psd/iasoa/sites/default/files/stations/nyalesund/nyalesund_site.jpg). However, the elevation difference and typical wind patterns largely prevent pollution from nearby sources to reach the Zeppelin Observatory. The dominating wind pattern is east-southeast katabatic flow from Kongsvegen glacier or from northwesterly directions as channeled by the Kongsfjord (Beine et al., 2001; Heintzenberg et al., 1983). The station itself was initially established in 1991, and is owned by the Norwegian Polar Research Institute (NP). The Norwegian Institute for Air Research (NILU) is responsible for the coordination of the scientific program.

2.1 Physical aerosol data

After a period of continuous aerosol measurements by the Department of Meteorology, Stockholm University in the early 1990ties, (Heintzenberg and Leck, 1994), the Department of Analytical Chemistry and Environmental Science, Stockholm University, initialized observations of the aerosol number size distribution in mid-2000. Originally, the system

157 consisted of a single differential mobility analyzer system, (DMPS), consisting of a medium-

158 size Hauke-type differential mobility analyzer, (DMA), together with a TSI 3760

159 condensation particle counter, covering diameters between 20 and ~500nm. From 2006 on

160 the particle size range was widened covering particle sizes between 10 and 790 nm. In 2005,

161 the rain-cover over the inlet was replaced. Initially, the instrument inlet was of a PM10 type,

162 removing particles or hydrometeors with diameters >10 μm from the sampled air stream.

163 During a substantial renewal of the Stockholm University equipment in 2010-2011, both inlet

164 and DMPS system were replaced.

165 Since then, the DMPS-system utilizes a custom-built twin DMA-setup comprising one

166 Vienna-type medium DMA coupled to a TSI CPC 3010 covering sizes between 25-800 nm

167 and a Vienna-type long DMA coupled with at TSI CPC 3772 covering sizes between 5-60

168 nm. The size distributions from the two systems are harmonized on a common size grid and

169 then merged. Both systems use a closed-loop flow setup. The current inlet hat is of whole air

170 type, complying with EUSAAR[1] standard for high altitude or Arctic sampling conditions. In

171 the current setup, the inlet is operated with a flow of ca. 100 liters per minute, (lpm). Laminar

172 flow conditions apply throughout the sampling lines. Outside of the station, the inlet

173 temperature is kept above 0°C using active heating. Inside the station the temperature

174 increases gradually to room temperature (maximum temperature reaches ca. 25 °C, but

175 remains typically around 20°C). Relative humidity, (RH) and temperature are internally

176 monitored and measurements are maintained at dry conditions with RH < 30%. The system is

177 regularly checked with latex spheres and flow controls. The recorded data are manually

178 screened and crosschecked with other available observation as in Tunved et al. (2013). If

179 inconsistencies were found between the different datasets, further investigation was

---

[1] EUSAAR (European Supersites for Atmospheric Aerosol Research) is an EU-funded I3
(Integrated Infrastructures Initiatives) project carried out in the FP6 framework of the specific
research and technological development gram "Structuring the European Research Area -
Support for Research Infrastructures", (http://www.eusaar.net/).

180   performed to exclude data that were identified as affected by instrumental errors. Using the

181   instrumental logbook, periods of local activity potentially influencing the sampling were also

182   excluded from the dataset. During the years 2006 – 2010 no particles below ten nanometers

183   in diameter were recorded. From 2011 on four more diameter bins down to 5 nm were

184   included and a different diameter array was utilized. To allow for a synopsis of all years all

185   size distributions were interpolated on the pre-2011 diameter array and all integrals of the size

186   distribution over particle diameter were taken over the joint diameter range 10 to 631 nm. For

187   the pre-2011 years the data at the four size channels below 10 nm were flagged as missing.

188   However, whenever results cover the complete time series the resulting number

189   concentrations in the four first channels covering the years 2011 – 2015 are carried along.

190   For the identification of NPF in terms of particle growth the parameter D50 in nanometer

191   was calculated as the number median diameter of particles smaller than 50 nm but larger than

192   10 nm, i.e. 50% of all particles below that size are smaller than D50. Besides this parameter

193   Table 1 lists nine integral particle parameters, which are utilized in the NPF-search

194   approaches or in the interpretation of results. These aerosol parameters quantify total particle

195   number, (NTO), and particle numbers in sub-ranges of the number size distribution such as

196   N25, quantifying the total number of particles between ten and 25 nm.

197   Following the concept developed by Pirjola et al., (1999), and Kulmala et al., (2001) we

198   calculated the condensation sink, (CS, s^{-1}), as a parameter with which the probability of new

199   particle formation from the gas phase and the necessary amount of condensable vapor can be

200   estimated. We utilized number size distributions, pressure and temperature taken from our

201   database for this calculation.

202

203

204

205

2.2 Chemical aerosol data

For the interpretation of NPF-events we employed chemical information derived from the analyses of high volume particle samples taken by the Norwegian Institute for Air research, (NILU). A high volume sampler (PM10) was used to collect samples for a quantitative determination of sodium, (Na^+), sulfate, (SO_4^{2-}) and MSA (CH_3SOO^-). The sampler collected material for analysis in one to three days. Blank samples were obtained by mounting the glass fiber filters at the sampling site with the same sampling period but without air passing through. Na^+ and SO_4^2 were analyzed by NILU and have been downloaded for the present study from the EBAS database (http://ebas.nilu.no), which list details about the sampling technique and the sampling protocol. Nss SO_4^{2-} was determined from total sulfate correcting for sea salt sulfate as $0.25 \times Na^+$, (Keene et al., 1986).

MSA was analyzed at the laboratory of the Department of Meteorology, Stockholm University. To allow for subsequent chemical determinations the ambient samples and blanks were carefully handled in a glove box (free from particles, sulfur dioxide and ammonia). At the time of the chemical analyses, still in the glove box, the substrates were extracted (in centrifuge tubes) with 60 cm^3 deionized water (Millipore Alpha-Q, conductivity 18 MΩcm). The extracts were thereafter analyzed for weak anions by chemically suppressed ion chromatography (IC, Dionex ICS-2000) using Dionex AG11/AS11 columns. In order to trap carbonates and other ionic contaminants a Dionex ATC-1 column was used before the injection valve. The injection volume was 50 μdm^3. Quality checks of the IC-analyses were performed with both internal and external reference samples (Das et al., 2011). The analytical detection limits obtained for the various ions, defined as twice the level of peak-to-peak instrument noise, was 0.0001 $\mu eq \ dm^{-3}$ for MSA. The overall analytical accuracy was better than 1.5%.

2.3   Back-trajectories and meteorological data

For every hour during the ten years 2006 through 2015 three-dimensional back trajectories have been calculated arriving at 474 m at Mt. Zeppelin. The trajectories have been calculated backward for up to ten days using the HYSPLIT4 model (Draxler and Rolph, 2003) with meteorological data from the Global Data Assimilation System with one-degree resolution (GDAS1). Trajectories extending backwards for ten days are inaccurate at origin due to the trajectory uncertainty of 25-30% of its length, (Stohl, 1998). More information about the GDAS dataset can be found at Air Resources Laboratory (ARL), NOAA (http://ready.arl.noaa.gov), from which the meteorological data were downloaded.

During the analyzed time period meteorological records at the Mt. Zeppelin station are rather limited in quality and were frequently interrupted. There are no precipitation measurements and wind measurements are strongly influenced by the station building and by the local topography. In order to have an internally consistent, and unbroken meteorological record we utilized hourly meteorological parameters at trajectory arrival times as calculated by the HYSPLIT4 model. We emphasize that their accuracy depends on the quality of the meteorological model inside HYSPLIT4 and the accuracy and representativeness of the meteorological fields utilized by the model. Of the local meteorological record air temperature was considered the most reliable and thus explored in a comparison of trajectory calculated and modeled meteorological data. When comparing the 42600 contiguous hourly records from 2008-01-01 until 2012-11-10 the average ratio of measured and calculated temperatures is 0.98, with a coefficient of determination of 0.96. The utilized model parameters are listed in Table 1.

As an additional parameter we evaluated the vertical air movement of the trajectories during the last hour before arrival by subtracting the trajectory height one hour before arrival

257 at the arrival height of 474 meter. The resulting vertical displacement parameter, DZ, is given

258 in meters per hour. Positive values of DZ indicate a lifting of the air.

259 The most important missing meteorological information concerns the local cloud cover.

260 No direct recording was available of times during which the station was in clouds. The

261 closest available cloud instrument is a ceilometer operated by the Alfred Wegener Institute

262 (AWI) at their Koldewey Station in Ny-Ålesund, i.e. in the valley below Mt. Zeppelin, some

263 2.8 km of horizontal distance from the position of the mountain station. From the one-minute

264 records of the ceilometer we derived hourly values of the 25% percentile of cloud base, which

265 was used as an indicator for the Zeppelin station being in cloud. This ceilometer parameter is

266 listed as C25 in Table 1.

267 Precipitating clouds scavenge the planetary boundary layer and thus reduce the available

268 particle surface as condensation sink of particle precursors. As a consequence nucleation

269 from the gas phase may be facilitated (Tunved et al., 2013). As in Tunved et al. (2013) we

270 utilized the HYSPLIT-modeled precipitation along the back trajectories. Sums of

271 precipitation, (SP, see Table 1), were calculated along each back trajectory and will be

272 referred to as SP1 (during the last day), SP2 (during the last but one day), and SP5 (during

273 days three to five) before arrival at Mt. Zeppelin.

274

275

276 **2.4 Marine biological data**

277

278 The biologically active marginal ice zone is a major natural source of sulfur in the Arctic

279 summer atmosphere, (Leck and Persson, 1996b, a), and Wiedensohler et al. (1996), indicated

280 a potentially important role of dimethyl sulfide (DMS) in regional new particle formation.

281 DMS emissions from the sea have long been proposed to control new particle formation in the

282 marine boundary layer, (Charlson et al., 1987), which builds on DMS_{aq} being transported via

283 turbulence and diffusion to the sea-air interface, represented by the transfer velocity, which in

284 turn depends on sea-surface temperature, salinity, and wind speed, (Liss and Merlivat, 1986).

285 Once in the atmosphere DMS_g is photochemical oxidized via intermediates such as sulfuric

286 acid and methane sulfonic acid, (Ayers et al., 1996), which eventually leads to the formation

287 of aerosol $nssSO_4^{2-}$ and MSA. The products of the photochemical oxidation of DMS the ratio

288 MSA/ $nssSO_4^{2-}$ show a temperature dependence (Bates et al., 1990), favoring MSA in the cold

289 Arctic environment (Karl et al., 2007).

290   Dimethyl sulfide in the ocean (DMS_{aq}) is produced through the degradation of its algal

291 precursor dimethylsulfoniopropionate (DMSP) by microbial food webs, (Simó, 2001). At

292 high latitudes, total DMSP (DMSPt) and therefore DMS_{aq}, essentially follows the seasonal

293 cycle of phytoplankton biomass, (Lana et al., 2012). DMSPt is defined as the sum of

294 $DMSP_{dissolved}$ and $DMSP_{particulate}$ concentration. Yet, the amount of DMSPt per unit

295 phytoplankton biomass may vary depending on species composition and physiological state,

296 (Keller et al., 1989).

297   The dissolved organic carbon (DOC) concentrations in surface waters of the high Arctic

298 Ocean are up to ten times higher than in any other ocean basin and closer in range to DOC

299 levels reported for sea ice (Gao et al., 2012). A large fraction of DOC spontaneously

300 assembles into polymer gels: polysaccharide forming hydrated calcium bonded three-

301 dimensional networks to which other organic compounds, such as proteins and lipids, are

302 readily bound. The assembly and dispersion of the polysaccharide molecules can be affected

303 by environmental parameters, such as UV-B radiation (280-320nm) dispersing or inhibiting

304 gel formation, and/or pH and temperature inducing gel volume phase changes (swelling and

305 shrinkage). In the study of Orellana et al., (2011b), the swelling and shrinking of the

306 polysaccharide networks or polymer gels were also causally related by additions of nano to

307 micromolar levels of DMS and DMSP. High DMSP concentrations have also been measured

308 in the mucilage surrounding prymnesiophyte *Phaeocystis pouchetii* colonies in Arctic waters,

309 representing up to 25% of the total water column DMSP pool, (Matrai and Vernet, 1997).

310 The findings made by Orellana et al., (2011b) were in agreement with previous findings by

311 Orellana et al., (2011a) that high concentrations of DMSP and DMS are stored in the acidic

312 secretory vesicles of the *Phaeocystis* algae where DMSP is trapped within the condensed

313 polyanionic gel matrix until the secretory vesicles are triggered by environmental factors such

314 as temperature to release gels that undergo volume phase transition and expand at the higher

315 pH of seawater. Exocytosis of polymer gels accompanied by elevated DMS and DMSP

316 concentrations suggests the transport of these chemical compounds by the gel matrix.

317 Schoemann et al., (2005) report that *Phaeocystis antarctica* is particularly well adapted to low

318 temperatures, being more competitive than *P. pouchetii for temperatures between -2* and

319 +2 °C. *Phaeocystis pouchetii*, however, appears to be better adapted to temperatures closer to

320 5 °C. In the Arctic a higher occurrence of the *Phaeocystis pouchetii* would be expected in the

321 northward advection of warm Atlantic water masses around Svalbard.

322 Here we estimated DMSPt at the sea surface using the algorithm described by Galí et al.

323 (2015). The DMSPt algorithm exploits the distinct relationship between DMSPt and

324 Chlorophyll-*a* depending on the light exposure regime of the phytoplankton community. The

325 light exposure regime is defined by the ratio between euphotic layer depth and mixed layer

326 depth (Z_{eu}/MLD). Additional predictor variables used are sea surface temperature (SST) and

327 particulate inorganic carbon (PIC), which is used in the algorithm as a proxy for

328 coccolitophores such as *Emiliania huxleyi*. During late bloom stages, the calcite plates that

329 cover coccolitophore cells (called coccoliths) detach and cause an increase in seawater

330 backscatter that invalidates satellite retrievals of Chlorophyll-*a*. Therefore, inclusion of PIC

331 in the algorithm as a proxy for DMSPt increases data coverage. Although the algorithm was

332 developed for the global ocean, validation results with in situ data indicate that it performs as

333 well or slightly better in Arctic and sub-Arctic waters.

334   The use of remotely sensed DMSPt as a proxy for marine DMSaq emission is a significant

335 improvement with respect to prior studies that used Chlorophyll-*a* (Becagli et al., 2016;

336 Zhang et al., 2015). Yet, it is not ideal because (i) the ratios DMS_{aq}/DMSPt in surface

337 seawater are variable, and tend to be higher in high solar irradiance and nutrient-poor

338 conditions typical of summer, (Galí and Simó, 2015), and (ii) even if DMSPt is a better proxy

339 for DMS_{aq}, the influence of meteorological and sea surface conditions (mainly wind speed

340 and SST) on the sea-air flux of DMS_{aq} is not taken into account. Development is underway of

341 an algorithm for the retrieval of DMS_g concentrations in air and DMS fluxes.

342   The DMSPt algorithm was run for the 2006-2015 period using daily composites of the

343 Moderate Resolution Imaging Spectroradiometer on the Aqua satellite (MODIS-Aqua) at 4.64

344 km resolution (L3BIN, reprocessing R2014.0) downloaded from NASA's Ocean Color

345 website (http://oceancolor.gsfc.nasa.gov). The MODIS variables used include Chlorophyll-*a*

346 concentration derived with the GSM algorithm, (Maritorena et al., 2002), PIC, nighttime SST

347 and Z_{eu}. MODIS nighttime SST was complemented with SST from the Advanced Very High

348 Resolution Radiometer (AVHRR, https://podaac.jpl.nasa.gov/AVHRR-Pathfinder) to increase

349 data availability. MLD was obtained from the MIMOC climatology, (Schmidtko et al.,

350 2013), which was linearly interpolated from its original 0.5°x0.5° grid at monthly resolution

351 to the MODIS grid at daily resolution.

352   Satellite remote sensing of biological activity in surface waters requires ice-free and at

353 least part of the time cloud-free. The passive sensing methods of MODIS additionally require

354 a minimum of solar illumination of the scenes (i.e., solar zenith angle < 70°; (IOCCG, 2015)).

355 Consequently, the length of the satellite-observable period used to compute DMSPt means

356 shortens from all-year-round at latitudes <45° to approximately six months (the spring-

357 summer semester) at 80°N. In addition, the annual DMSPt map in Fig. 3 excludes all land and

358 ice covered regions. In order to increase data coverage, daily DMSPt composites were binned

359 to five-day periods and a 46.4 km equal-area sinusoidal grid, (10x10 bins of the original pixel

360   size). The average distance between a trajectory point and the closest center of a MODIS

361   pixel is 18 km.

362   Following the same approach as with the ice data average DMSPt from ocean color data,

363   (OC), along each back trajectory were calculated and will be referred to as OC1 (the last day),

364   OC2 (the last but one day), and OC5 (days three to five) before arrival at Mt. Zeppelin. In

365   this procedure missing data were flagged as such, and were not taken into account.

366

367

368   **2.5   Ice data**

369

370   For the interpretation of events of new particle formation observed during the *Oden* cruises

371   information on pack ice extent under the air masses reaching the sampling points proved

372   crucial (Heintzenberg et al., 2015). Another motivation for utilizing ice data in the present

373   study is the fact that the Svalbard region experiences large seasonal changes in pack ice cover

374   which we expect to have strong effects on emissions of particles and their precursor gases.

375   Thus daily ice concentrations were taken from the NSIDC database (https://nsidc.org/data).

376   The irregularly shaped data gap around the pole caused by the inclination of satellite orbits

377   and instrument swath was filled with 100% cover. To each hourly position and data of the

378   back trajectories the ice information in the corresponding maps of ice concentrations were

379   added and displayed in Fig. 2. On average the closest pixel in the ice maps was about 12 km

380   off any trajectory point.

381   In the discussion of results we utilize the complement of ice cover, i.e., the amount of open

382   water because the marine biological processes of interest predominantly take place in the

383   open water, (Leck and Persson, 1996a). As integral parameters average open water, (OW),

384   percentages along each back trajectory were calculated and will be referred to as OW1 (the

385   last day*)*, OW2 (the last but one day), and OW5 (days three to five) before arrival at Mt.

386   Zeppelin. The most solid ice cover is seen in an area reaching from Northeastern edge of

387   Greenland via North Pole to Parry Island. A marginal ice zone extends along the east coast of

388   Greenland to Franz-Josef-Land, and the area between Svalbard and the latter island.

389

390

391   **2.6   ERA-Interim data of sea surface temperature**

392

393   Daily Sea Surface Temperature (SST) data for our study period (2006-2015) were

394   downloaded from the website of the European Centre for Medium-Range Weather Forecasts

395   (ECMWF). A description of the global atmospheric reanalysis, (ERA-Interim), has been

396   given by Dee et al. (2011), and a guide to the products and the download procedures can be

397   found at   http://www.ecmwf.int/en/elibrary/8174-era-interim-archive-version-20.   Briefly,

398   ERA-Interim is an assimilating model reanalysis of the global atmosphere and sea-surface

399   physical parameters covering the data-rich period since 1979. SST data were downloaded at a

400   resolution of approximately 0.56° and regridded onto the same 46 km equal-area sinusoidal

401   grid used for DMSP and cloud fraction, (see below). Ice-covered pixels were screened out

402   prior to the back-trajectory analysis. In the Arctic region, ERA-Interim has been shown to be

403   a top performer among a number of atmospheric reanalyses, (Lindsay et al., 2014).

404

405

406   **2.7   MODIS cloud fraction**

407

408   Persistent cloud cover limits PPP in Arctic and Sub-arctic seas, (Bélanger et al., 2013), and,

409   as mentioned above, irradiance at the sea surface, which is largely controlled by cloudiness,

410   influences $DMSP_{dissolved}$-to-DMS_{aq} conversion. Boundary layer clouds are known to be

411   additional controllers of the surface aerosol (Heintzenberg, 2012). In the summer Arctic low

412 level clouds and fogs are widespread (Warren and Hahn, 2002). Both scavenging and new

413 particle formation have been observed in connection with low clouds and fog passages

414 (Lannefors et al., 1983; Heintzenberg and Leck, 1994; Leck and Bigg, 1999; Heintzenberg et

415 al., 2006; Karl et al., 2013). Beyond the cloud base derived from the ceilometer we have no

416 other in situ local or regional cloud information. Thus, we utilize satellite-derived cloud

417 information.

418 Daily Level-3 global cloud fraction with one-degree resolution was downloaded from

419 NASA website (http://modis-atmos.gsfc.nasa.gov, Hubanks et al., 2015) and extracted for our

420 region of interest. Briefly, level 3 images correspond to the aggregation of all level 2 images

421 (1 km resolution) available within the one-degree resolution grid. For a given L2 scene, each

422 pixel is assigned a value of 1 (cloudy) or zero (clear sky), and then the individual scene values

423 are averaged over a 24-hour period. Note that a given pixel can be revisited up to six or seven

424 times in the course of a day at high latitudes. Finally, the daily composites were re-projected

425 to 46.4 km pixels to match the spatial resolution of DMSPt. The average distance between a

426 trajectory point and the closest MODIS pixel was 18 km.

427 The cloud fraction CF as well as other cloud properties from MODIS have been

428 extensively used, for instance to study the global spatial and temporal distribution of clouds

429 over the last decade (e.g., King et al., 2013). Several studies have also successfully

430 performed validation by comparison with in situ data (e.g., An and Wang, 2015) which

431 demonstrated the ability of the MODIS-aqua sensor to retrieve cloud cover.

432 Following the same approach as with the ice data and DMSPt, average cloud fractions,

433 (CF, see Table 1), along each back trajectory were calculated and will be referred to as CF1

434 (the last day), CF2 (the last but one day), and CF5 (days three to five) before arrival at Mt.

435 Zeppelin. Missing data are flagged as was done with DMSPt data.

436

437

438 **3. Three approaches to identifying events of new particle formation**

439

440 There are no definitive and no generally accepted methods to identify or predict NPF-events

441 in atmospheric time series of aerosol data. Thus, in the present study we explored different

442 approaches with varying degrees of complexity to identify such events. We emphasize that

443 none of these approaches explicitly is connected to diel cycles such as in Dal Maso et al.,

444 (2005) or makes any assumptions about the time of day during which new particle formation

445 occurs. Three objective search algorithms were written in FORTRAN to analyze the time

446 series of hourly records of aerosol parameters in search of new particle formation:

447 1. The simplest approach of upper percentiles (PCT-approach), assumes that NPF-events are

448   characterized by extremely high concentrations of small particles in terms of N25 (see

449   Table 1). The key parameter characterizing each PCT-event was the value of N25

450   averaged over a fixed number of hours, ($N25_{av}$), after the nominal start of an event, (see

451   below). With $N25_{av}$ also a nominal length of PCT-events was defined as the number of

452   hours after the start of an event by which N25 sank to less than half of $N25_{av}$.

453 2. The more specific approach of diameter growth (DGR-approach) builds on the temporal

454   development of the particle size distribution in terms of a systematic growth of the

455   diameter D50 (see section 4.1) to find the classical "Banana Type" of NPF-event,

456   (Kulmala et al., 2004). The key parameter characterizing each DGR-event was the average

457   growth of D50 during the nominal event length NUC, (see below). For this approach the

458   nominal length of events was reached when the running two-hour average growth fell

459   below the value one.

460 2. The most complex approach of multiple-size events, (MEV-approach), searches for events

461   with concurrent appearance of concentration increases in several size classes below 60 nm

462   diameter (Karl et al., 2013; Leck and Bigg, 2010). The key parameter characterizing each

463   MEV-event was the relative concentration increase averaged over the chosen size classes

464   below 60 nm during the nominal event length NUC, (see below). As with PCT-events a

465   nominal length of MEV-events was defined as the number of hours after the start of an

466   event by which N25 sank to less than half of $N25_{av}$.

467

468 Three time-related parameters were commonly defined for all three approaches:

469 1. Nominal NPF-event length, (NUC) was nine hours.

470 2. Pre-event periods, (PRENUC), from which increases in diameters or number

471   concentrations were calculated, were six hours.

472 3. Reference periods, (REF), before PRENUC and after NUC periods were defined in order

473   to compare event and pre-event data with non-event conditions. Each of these reference

474   periods had the length of half the sum of pre-event plus event time periods, making the

475   total reference time period of each event as long as that of the event itself.

476 Besides these common characteristic lengths individual fixed thresholds were chosen and

477 discussed below for each approach in order to generate at least 200 unique events per

478 approach, (see Table 2).

479   The aerosol data used to define the NPF-events were complemented by a large number of

480 environmental parameters. The primary temporal resolution of the environmental parameters

481 was between one minute (C25, cf. Table 1) and five days (DMSPt, cf. Table 1). C25 was

482 calculated as 25% percentile on an hourly basis. The parameters with resolutions higher than

483 an hour (OW, CF, and OC, cf. Table 1) were evaluated along the hourly back trajectories.

484 While this procedure yielded hourly varying results even of OW, CF, and OC it has to be kept

485 in mind that this hourly variability is the result of hourly resolved trajectories traversing the

486 grid; the low primary temporal resolutions of the OW, CF, OC, and chemical parameters

487 remain. For these slowly varying parameters the REF periods before and after the events

488 were extended to one day beyond the longest primary resolution, i.e., six days.

489   For two reasons the three search algorithms may yield temporarily redundant results, i.e.,

490   they may identify the same events. One, they go independently through the same time series

491   of aerosol data, possibly causing inter-approach redundancy. Two, each algorithm goes

492   through the time series hour by hour, thus allowing for temporal overlap of events found by

493   each approach, (intra-approach redundancy).

494   The three types of events were assumed to be mutually exclusive and potentially being

495   caused by different sets of conditions for new particle formation. Thus, a FORTRAN

496   procedure was developed to eliminate both intra and inter-approach redundancy while

497   maintaining a maximum of identified NPF-events. To remove intra-approach redundancy the

498   procedure identifies overlapping events within each approach. Of each ensemble of such

499   overlapping events the one with the strongest key parameter of the respective approach

500   (growth of D50, or concentration increases as defined above) is retained. Next, inter-

501   approach redundancy is addressed by the procedure. However, there is no unique solution to

502   the problem of the partly redundant three time series of events. In order to avoid any

503   preference of one or several types of events in the tests of inter-approach overlap pairs of

504   events of different approaches are chosen at random and compared for overlap. This random

505   comparison is done as often as the product of the number of events of the three approaches.

506   This rather time-consuming random test yields stable numbers of non-overlapping events

507   within less than one percent, irrespective of the order in which the events of the three

508   approaches were arranged for the test. By removing intra and inter-approach redundancy in

509   the first two steps of the procedure a number of time periods will be "freed". Consequently,

510   in a last step, the procedure tries to fill the "freed time periods" non-redundantly with events

511   of the three approaches that had been eliminated in the first two steps. Table 2 collects total

512   numbers and unique numbers of events for each approach. In the rest of the paper only non-

513   redundant events will be discussed. The total number of new particle formation events will

514   be shortened to TNPF.

3.1 The upper percentile of N25 (PCT-approach)

Events of new particle formation were identified by time periods in which N25 was consistently, i.e. on average for three hours, above a set threshold. With a threshold of the 93%-percentile (170 cm^{-3}) 4143 PCT-events were identified in the total data set, only 240 of which were unique because most of them overlapped with event or pre-event times of the other two approaches. Average N25 during these unique events was 330 cm^{-3} and the average length of events 4 ±0.9 h, (one standard deviation).

Fig. 4, (top), shows the average temporal development of the relative size distributions for the unique PCT-events as in the results in Karl et al. (2013), i.e. relative concentrations were formed by dividing the absolute number concentrations by the average total number during the six-hour pre-event time periods. The events are characterized by a nearly monomodal distribution around 20 nm that broadens somewhat around the nominal start of the events. During the last three hours before the events D50 decreased slightly and returned to the pre-event level during the nine NUC hours.

In connection with PCT-events average aerosol parameters NTO through N300 showed an average increase by a factor of 2.2 during PRENUC-periods, which was maintained on an average level of 1.5 during the events. The aerosol-chemical parameters Na$^+$, nssSO$_4^{-2}$, and MSA were on an average level of 20% of their reference value. The average environmental parameters indicate a strong increase by a factor of 14 in solar radiation and a lifting of cloud base before the events. During the events the level of solar radiation was still elevated by a factor of six above its reference value. As a consequence temperature at the station was up by 2 – 3 degrees. Precipitation 12 h before trajectory arrival time, (SP12) was a factor of five above reference levels for air arriving during NUC-periods, whereas SP35 to SP5D were below their respective reference levels. Cloud fractions were slightly raised 12 - 48 h before air arrival. Of the ocean parameters more open water was met by trajectories 12 to 24 before

541 their arrival with ocean temperatures 12 to 48 h before trajectory arrival having been up to

542 four degrees warmer than their respective reference values. On average DMSPt-parameters

543 OC24 through OC5D showed were raised by a factor of two above their reference value.

544   In Fig. 5, (left top panel), average trajectory height profiles during PRENUC and NUC-

545 periods are displayed. Widely varying vertical air mass paths occurred before and during

546 PCT-events. Median vertical trajectory paths during PRENUC and NUC times indicated air

547 coming from some 300 m above station level five days ago sinking to about one hundred

548 meters above station level during the last two days before arrival. The upper quartiles of the

549 PCT-height profiles point at strong subsidence before air mass arrival.

550   The right top panel in Fig. 5 maps average horizontal trajectory positions in 12 h steps in

551 months having at least ten PCT-events, i.e., May - September. Filled circles around the

552 trajectory positions comprise 95% of all events. The monthly average horizontal trajectory

553 direction during PCT-events mostly was from the northwest. In June and July the trajectories

554 reached farthest into the multiyear ice cover northeast of Greenland. Only during September

555 the back trajectories covered ice-free and marginal ice areas in the Fram Strait. We note that

556 the five-day back trajectories of PCT-events, (and of the other two approaches as well), stayed

557 within some 800 km of Mt. Zeppelin.

558

559

560 **3.2   The diameter growth (DGR) approach**

561

562 The DGR-approach to identify events of new particle formation builds on the classical

563 concept of particle growth through condensable vapors after an initial nucleation of sub-five

564 nanometer particles that cannot be observed with the available instrumentation, so called

565 "Banana-type" (Kulmala et al., 2004). The respective algorithm utilizes the parameter D50,

566 (see Table 1), and requires a growth of this diameter by at least a factor of 1.5 after the

567   nominal start of an event. With this threshold the algorithm searched through all 87646 hours

568   of the ten-year record and found 1199 DGR-events of new particle formation. After

569   eliminating cases of temporal overlap with the other two approaches 235 unique events of this

570   type remained, (see Table 2). Other or more DGR-events could have been found by

571   shortening the nominal nine NUC hours. For two reasons we refrained from discussing

572   shorter growth periods in the DGR-approach. Maintaining common-length NUC periods

573   facilitated the comparison of results of the three approaches. Furthermore, reducing the

574   growth period would also make PCT and DGR-events ever more similar.

575   Starting with an average value of $D50 \approx 16$ nm at the nominal start of DGR-events an

576   average growth rate of 1.8 nmh^{-1} is derived, which is in the range of $1 - 2$ nmh^{-1} derived by

577   Ström et al. (2009) for new particle formation in the lower boundary over Ny-Ålesund,

578   Spitsbergen but considerably lower than the maximum growth rate of 3.6 nmh^{-1} reported by

579   Asmi et al. (2016) for July at the Siberian station Tiksi at the coast of the Laptev Sea. For

580   open ocean new particle formation events over the North Atlantic O'Dowd at al. (2010) report

581   a "typical growth rate" of 0.8 nmh$^{-1,}$ whereas Ehn et al. (2010) give an average growth rate of

582   3 nmh^{-1}. The average length of DGR-events was 10 ±1 h, (one standard deviation).

583   The average temporal development of the relative number size distribution during DGR-

584   events is presented in Fig. 4, (center). After a decrease of the sub-50 nm diameter median

585   from about 25 to 16 nm during the six hours before the nominal start of the events D50

586   increases systematically during the following nine NUC hours with somewhat reduced growth

587   towards the end of the event.

588   During the PRENUC-periods particle number concentrations N300, and the condensation

589   sink, (CS), decreased relative to the reference periods before and after the events.

590   Subsequently, during the NUC periods the strongest increases was found for N60.

591   Environmental parameters around air mass arrival showed a strong lifting of cloud base,

592   (C25), and an extremely high increase in solar radiation, (by a factor of 11 during PRENUC

593   and by a factor of 60 during NUC periods). However, 12 h before air arrival precipitation had

594   been up by a factor of 2.5. Cloud fractions were down to about 70% of their reference values

595   24through 48 h before air arrival. Of the chemical aerosol parameters Na^+ and $nssSO_4^{-2}$

596   showed an increase of 2.6 and 2.3, respectively. OC12 and OC48 were slightly higher than

597   reference level before and during the events. Sea surface temperatures T24 were raised by

598   nearly one degree whereas earlier SST-values, (T36 – T5D), were up to one degree below

599   reference values.

600   Fig. 5, (left center panel), shows statistics of the vertical air movement before trajectory

601   arrival during DGR-events at Mt. Zeppelin covering a wide range of vertical movements

602   between 200 m and beyond 1500 m height. During the days when elevated DMSPt levels

603   were noted median trajectory heights were six to nine hundred meters. Median trajectories

604   during PRENUC times dipped down to the station level, (474 m a.s.l), about one day before

605   arrival, albeit lifted and subsided again shortly before arrival. Vertical trajectory pathways

606   will be discussed further in Section 4.2.

607   Monthly average trajectory positions and their variability in connection with DGR-events

608   are shown in Fig. 5, (center right panel). The months April through October had at least ten

609   DGR-events per month. As with PCT-events the general trajectory direction was from the

610   northwest, mostly staying for several days over the marginal ice zone between northeastern

611   Greenland and eastern Svalbard. During the earliest month of April with 14 DGR-events the

612   back trajectories reached farthest south into the ice-free parts of the Fram Strait.

613

614

615   **3.3   The Multiple-size approach (MEV)**

616

617   Leck and Bigg (2010) and Karl et al. (2013; 2012) discussed a type of new particle formation

618   that to date only has been reported from the summer Arctic. During these MEV-events high

619   ultrafine particle concentrations appear concurrently in a broad diameter range reaching from

620   under 10 to some 60 nm. We simulated this type in a search that required the concurrent

621   increase of NTO, N20, N40, and N60, (cf. Table 1), as averaged over the first three NUC

622   hours by a factor ≥ 1.6 over their respective averages during the six (PRENUC) hours. Over

623   the ten years of data 1191 such events of this type were identified, 266 of which remained

624   after removal of those overlapping with events of other approaches. During these unique

625   events the average concurrent concentration increase was 4.7 and the average length of the

626   events 12±0.8 h.

627   The concurrent appearance of high concentrations at many particle sizes below 60 nm

628   resembles the nocturnal NPF-events analyzed by Suni et al. (2008) in the Australian

629   Eucalyptus forest and simulated in subsequent chamber experiments (Ristovski et al., 2010;

630   Junninen et al., 2008). We emphasize though that the condensing vapors in the Australian

631   NPF-events originating from terrestrial biogenic emission are quite different from the

632   polymer gels implicated in the Arctic MEV-events and originating from the surface

633   microlayer of the ocean.

634   The bottom part of Fig. 4 shows the average temporal development of relative number size

635   distributions before and during MEV-events. The development before the nominal start of

636   MEV-events is more complex than during the PRENUC-periods of the first two types of

637   events. Intermittently a mode around seven nanometers shows up that broadens and becomes

638   more prominent about two hours before the nominal start of events. The major PRENUC-

639   mode around 25 nm also broadens and becomes more prominent towards NUC. A weak

640   mode exists during PRENUC around 120 nm and hardly any particles beyond 400 nm. D50

641   sinks from 25 to about 20 nm and stays below 25 nm through the MEV-events even though

642   number concentrations increase during the first NUC-hours by more than a factor of five.

643   During NUC-periods all particle number concentrations increased, on average by a factor

644   of 1.6. Average solar radiation also increased by about 90% above reference level during

645 NUC-periods. Of the chemical parameters $nssSO_4^{-2}$ showed an increase by a factor of three

646 during PRENUC and NUC-periods, and MSA a slight increase during PRENUC-periods. On

647 one hand, precipitation 12 h, and 36 to 48 h before trajectory arrival, (SP12, SP48), were

648 above reference levels for air arriving during PRENUC-periods. On the other hand, during

649 PRE, SP24, SP36, an SP5D indicated dry conditions during PRENUC and NUC-periods.

650 Only three to five days before air arrival slightly increased cloud fractions were noted. Sea

651 surface temperatures up to five days before trajectory arrival were on average about one

652 degree lower than their reference values. DMSPt parameters OC12 to OC36 were raised by

653 factors of 1.3 and 1.6 during PRENUC and NUC-periods, respectively.

654 Percentiles of vertical trajectory coordinates prior to and during MEV-events are displayed

655 in Fig. 5, (bottom left panel). During the events, and even stronger during the PRENUC

656 periods median trajectories had been below 500 m for more than four days. Furthermore, the

657 final air approach to Mt. Zeppelin mostly came from below the station level. Upper quartiles

658 of the vertical trajectory positions are substantially lower than with DGR-events. We note,

659 however, that a short excursion above station level occurred in the upper quartiles during the

660 last three hours before arrival.

661 The bottom right panel of Fig. 5 gives the monthly average trajectory positions and their

662 variability in connection with MEV-events. The months April through October had at least

663 ten MEV-events per month. As with the other approaches the general trajectory direction was

664 from the northwest, albeit with stronger swings towards the ice-free areas south of Svalbard

665 early and late in the season, (April, May, and September). Interestingly, the trajectories of the

666 11 MEV-events in October were directed nearly straight north from the North Pole.

667 Summarizing differences and commonalities among the results of the three approaches we

668 can state that the length of the events increases from four to ten and twelve, going from PCT

669 to MEV-events. PCT-events are characterized by lower-than-reference aerosol-chemical

670 parameters. Na^+ and $nssSO_4^{-2}$ show strong increases in the other two types of events: Na^+ in

671 connection with DGR-events and $nssSO_4^{-2}$ in connection with MEV-events. Both, PCT and

672 DGR-events exhibit strong increases in solar radiation. Precipitation before air arrival was

673 raised at varying times in connection with the three types of events. Cloudiness both

674 increased and decreased at varying times before air arrival with the three types of events.

675 Increased open water under the trajectories was strongest with DGR-events and least

676 important with MEV-events. Only in connection with PCT-events strongly raised sea surface

677 temperature were noted before trajectory arrival. DMSPt related ocean parameters were

678 raised to varying degrees and at varying times before all NPF-events, most strongly in

679 connection with PCT-events and least in connection with DGR-events.

680

681

682 **4. Discussion**

683

684 **4.1. Environmental setting**

685

686 The discussion of the results on new particle formation in the Svalbard region builds on the

687 variability of new particle formation and related environmental parameters on scales of

688 months, and days. Fig. 1 gives an overview over the geographic areas which were covered by

689 one, two, and five-day back trajectories to Mt. Zeppelin during the ten years of the present

690 study covering the months March through October. This figure illustrates that air arriving at

691 Mt. Zeppelin during the ten summers of the present study came from widely varying regions

692 from the central ice-covered Arctic via the northern seas and northernmost Scandinavia to

693 Greenland. One-day back trajectories cover a roundish area from the central east coast of

694 Greenland via northern Scandinavia to Franz-Josef-Land, North Pole and back to the north

695 coast of Greenland. Excluding inner Greenland this area is widened by roughly 500 km by 2-

696 day back trajectories and by at least another 500 km by 5-day back trajectories reaching over

697   most of Greenland and the adjacent seas west of Greenland. This is a much wider region

698   from which air may reach Mt. Zeppelin as compared to sites in the inner Arctic as illustrated

699   in Fig. 2 of Heintzenberg et al. (2015).

700   On the path of trajectories to Mt. Zeppelin quite different ice conditions were met (see,

701   Fig. 2). On average North Atlantic open waters reached around West Spitsbergen all the way

702   to Nordaustlandet.   Drift ice was passed over by trajectories along the whole east coast of

703   Greenland. One-day trajectories passed over the marginal ice zone from the Fram Strait to

704   Franz-Josef Land but also over more contiguous ice close to the North Pole. At times, with

705   five-day back trajectories, even the marginal ice regions of Baffin Bay and Beaufort Sea were

706   reached.

707   The long-term geographical distribution of DMSPt in Fig. 3 reflects the water conditions

708   for phytoplankton biomass around Svalbard. Directly at the coasts of Greenland and Eurasia

709   increased nutrient availability in coastal and shelf waters (due to continental run-off and

710   enhanced hydrodynamics) cause localized areas of high DMSPt values. The low DMSPt

711   values further out along the coast of Greenland are due to sea ice reaching through the Fram

712   Strait far south, (see Fig. 2). A prominent feature in the regional DMSPt distribution is the

713   tongue of high DMSPt, (intense blue color), and thus high phytoplankton biomass east of this

714   area, reaching from Spitsbergen to roughly Jan Mayen that lies within one-day back

715   trajectories. Northward-flowing Atlantic waters, carried by the West Spitsbergen Current,

716   and southward-flowing fresh surface waters from melting ice, and recirculated Atlantic

717   waters, carried by the East Greenland Current (Rudels et al., 2005) are meeting. The layering

718   created by water masses of different density stabilizes the water column and traps

719   phytoplankton cells at well-lit depths. If sufficient nutrients are available, this can lead to the

720   development of large phytoplankton blooms, which can result in high concentrations of

721   DMS_{aq}, (see Fig. 2 in Leck and Persson, 1996a).

722   In the ten-year average cloud fractions systematic differences in cloudiness appear.

723   Depending on transport pathways as identified by the back trajectories, cloudiness varies on

724   the way to Spitsbergen. The ice-covered areas, (cf. Fig. 2), from the east coast of Greenland

725   to Franz-Josef-Land exhibit somewhat lower cloud fractions than the ice-free regions

726   southwest to east of Spitsbergen.

727

728

729   **4.2   Seasonal variability**

730

731   Seasonal changes are discussed in terms of monthly averages taken over the ten-year study

732   period. As expected in Earth's polar regions the seasonal variability of all environmental

733   parameters is very high as exemplified by the solar flux, (SFL), and the air temperature,

734   (TEM), at Mt. Zeppelin in Fig. 6. Due to the seasonal change in cloudiness, (cf. Fig. 7), the

735   seasonal distribution of SFL is not quite symmetrical about midsummer but is skewed slightly

736   towards the cloud minimum in spring. The air temperature, however, does not peak before

737   July and has a broad shoulder into fall and winter. The first, and partly absolute maxima, of

738   the seasonal distributions of NPF-events in Fig. 6 coincide with that of the SFL but then drop

739   of more slowly towards fall than solar radiation. In particular, MEV-events do so and even

740   have their main maximum in August. The occurrence of all NPF-events drops off sharply in

741   October. Whereas May as the first month with larger numbers of events is dominated by

742   PCT-events, followed by DGR and then MEV-events, the contributions of the three NPF-

743   types are reversed in the last month with high NPF-numbers, i.e., September.

744   Fig. 6 clearly shows that the formation of new particles in the Svalbard region is not

745   controlled by the late winter-to-early-spring phenomenon of Arctic haze peaking with highest

746   sulfate-concentrations in March, (cf. Fig. 3 in Heintzenberg, 1989, and Fig. 6), which has a

747   minimum in the total number of NPF-events. This minimum is in contrast with the maximum

748 in new particle formation rates found by Croft et al. (2016a) with their global aerosol model.

749 The high numbers of accumulation mode particles during the Arctic haze months in late

750 winter and spring yield the annual maximum in condensation sink, (CS in Fig. 6), which

751 could quench nucleation events and subsequent growth. Thus, even though photochemistry

752 may produce significant amounts of nucleating material, the freshly formed particles will not

753 grow to stable size before they are removed via either deposition or coagulation as discussed

754 by Tunved et al. (2013) and others. An alternative explanation of the late onset of NPF-

755 events in TNPF in spring lies in the marine biological processes not being activated nearby

756 during the Arctic haze period yet, (Heintzenberg and Leck, 1994).

757 Fig. 7 collects the seasonal variation of environmental parameters as averaged along the

758 back trajectories to Mt. Zeppelin. From their minimum in March-April open water conditions

759 improve until September, after which the pack ice extent under the trajectories rapidly

760 increases again. The widening open water areas are reflected in sea surface temperatures

761 under the trajectories that increase until September before they drop off strongly in October.

762 Consequently, because of its connection to marine biological activity DMSPt increases in the

763 euphotic zone from first photosynthetic light in May until it evens out around July and drops

764 off in October. Largest DMSPt values are reached in the vicinity of Svalbard, (cf. OC12 in

765 July and August in Fig. 7), i.e. considerably later than MSA. The ending of DMSPt-curves in

766 October is due to the lack of data not due to zero-DMSPt. Still, DMSPt concentrations are

767 expected to be low at this time of the year at temperate to polar latitudes due to low

768 phytoplankton biomass and low light exposure, (see Fig. 9 in Galí et al., 2015). In terms of

769 the MODIS-derived cloud fraction cloudiness increases rapidly from its minimum in April

770 and evens out on a plateau of $80-90\%$ after July. The spring-minimum in cloudiness is

771 confirmed by the maximum in cloud base as indicated by C25 in Fig. 7. This seasonal

772 distribution of cloudiness does not correspond to the classical picture of near-surface

773 cloudiness that exhibits near cloud-free conditions in winter and mostly overcast with Arctic

774 stratus and fogs during the summer months (Warren and Hahn, 2002; Huschke, 1969). We

775 explain the difference by the specific atmospheric pathways covered by the back trajectories

776 of the present study (cf. Fig. 1). Trajectory-averaged precipitation parameters (SP12-5D in

777 Fig. 7) have minima in the period April – May, from which they increase towards their

778 maxima in fall and winter.

779   The chemical aerosol information derived from the analyses of filters samples has a

780 relatively low temporal resolution of at least one day combined with frequent gaps of several

781 days in between samples. Thus, it cannot directly be related to the time periods of NPF-

782 events. The seasonal distribution of chemical tracers, however, yields important information

783 about new particle formation. Taken over the whole year $nssSO_4^{2-}$ in Fig. 6 is largely

784 anthropogenic, (Heintzenberg and Leck, 1994), and has its maximum during the peak of

785 Arctic haze in March and April and its minimum in August, which does not match any

786 seasonal distribution of NPF-events. We also plotted Na^+ in Fig. 6 as a tracer of the inorganic

787 marine aerosol components sea salt. Na^+ decreases from its winter maximum to its summer

788 minimum in June/July, again without similarity to the NPF-distributions. Instead, the

789 seasonal distribution of Na^+ rather closely follows that of the trajectory-derived wind speed

790 during the last hour before arrival, (not shown in the figure). Wind speed as driver for sea salt

791 production is a well established phenomenon (Blanchard and Woodcock, 1957). After a steep

792 rise in April MSA in Fig. 6 sharply peaks in May and then gradually drops off towards its

793 minimum in October, more gradually than reported for data taken from 1991 to 2004 by

794 Sharma et al. (2012) and earlier than reported by Heintzenberg and Leck (1994), both at the

795 same station. Our seasonal distribution of MSA most closely resembles that of SFL, in Fig. 6,

796 albeit with its peak in May a month earlier that SFL and more strongly skewed towards

797 spring. According to Leck and Persson (1996b) on average the concentrations of the marine

798 biogenic sulfur components, (DMS and MSA), fell with a decline rate of about 30% per week

799   approaching zero values in September explained by reduced ppp (Leck and Persson, (1996a),

800   (consistent with Becagli et al., 2016).

801   As MSA is the only measured aerosol component with exclusively marine biogenic

802   sources, we illustrate its seasonal distribution in greater detail in Fig. 8. In this figure MSA-

803   concentrations measured on Mt. Zeppelin have been extrapolated along 5-day back

804   trajectories, forming monthly average monthly maps of potential MSA-sources during the

805   biologically most active months of March through October.

806   Fig. 8 yields several pieces of information that are relevant to the issue of new particle

807   formation. Early in spring the biological aerosol sources are limited to the North Atlantic and

808   Norwegian Sea. In April the tongue of newly opened waters between Novaya Zemlya and

809   Franz-Josef-Land seemingly is beginning to become biologically active. In May this area

810   widens towards the Barents Sea while the North Atlantic also becomes more active, reaching

811   the Fram Strait. In August two wide potential source regions cover the region from Northern

812   Greenland to the northern end of Scandinavia and the region Barents to Kara Sea. In

813   September even the pack ice north of Svalbard becomes biologically active, (Leck and

814   Persson, 1996a), and shows potential MSA sources, in particular, north of the northern coast

815   of Greenland. Finally, the very weak potential MSA sources in October appear to be situated

816   mainly over the Kara Sea and over the North Atlantic.

817   How do these seasonal distributions compare to those of the NPF-events identified by the

818   three search-approaches defined in Section 3? To address this question we constrained the

819   average seasonal distribution of environmental parameters to those hours that had been

820   identified by the NPF-events of the three approaches. However, none of the individual

821   seasonal distributions of constrained environmental parameters follows closely any of the

822   NPF-events. In particular, the main MSA peak remains in May, thus one month earlier than

823   any peak of the NPF-occurrences. To elucidate further potential differences in the three types

824   of NPF-events we return to the discussion of vertical pathways of related back trajectories,

825   (see Fig. 5). In this figure all three types of NPF-events exhibit a wide range of vertical

826   trajectory paths. As we expect the regional sources of primary particles and particle

827   precursors to be at or near the surface we segregated the NPF-events into subpopulations with

828   back trajectories that remained a given time below 500 m, (roughly station level). In Fig. 9

829   we collected the results concerning the 93 NPF-events that occurred with trajectories under

830   the 500 m limit, i.e., roughly 12% of all events. The top panel shows that the related

831   trajectories not only stayed below 500 m through most of the last five days before arrival but

832   close to the surface until they started rising to the station level about 24 h before arrival. The

833   peak of the sum of event occurrences now coincided with the main MSA peak in May, (see

834   center panel in Fig. 9). For DGR-events the May-maximum was particularly strong whereas

835   the PCT-predominantly occurred in May and June and MEV-events remained clustered

836   around the later part of summer, possibly coupled to SST and DMSPt.

837   A number of environmental parameters indicated substantial deviations from their

838   respective reference values during the months with most frequent occurrence of this sub-

839   population of NPF-events. Strongest deviations were noted for precipitation that was elevated

840   above reference levels two to five days before trajectory arrival, most prominently for DGR-

841   events in May, (by a factor of six 36 h before trajectory arrival). Strong positive deviations in

842   aerosol-chemical parameters only occurred with Na^+ in PCT and MEV-events, indicating

843   relatively high wind speeds near sea surface in the related air masses. MSA was elevated up

844   to 50% above reference levels only during MEV-events. Elevated levels of DMSPt were

845   noted with all three types of NPF-formation, most prominently for DGR-events 12 to 36

846   hours before which DMSPt was increased by a factor up to 1.7 relative to reference levels.

847   The bottom panel of Fig. 9 gives average trajectory positions in 12 h steps for the months

848   May through September. The circles around the steps comprise 95% of all trajectories.

849   During all months the trajectories stayed in the ice-free and marginal ice zone between Fram

850   Strait and Eastern Svalbard as illustrated by average July ice cover for the ten study years,

851 (for average monthly ice covers cf. Fig. 8). In particular during the earliest and latest months

852 of May and September the trajectories swing farthest south over the open water south of

853 Svalbard. We note that the complementary sub-population of results with trajectories

854 remaining above station level did not yield results that differed strongly from those for the

855 whole population of back trajectories.

856 As a last step in the discussion of seasonal variations in new particle formation a model is

857 formulated that describes the average sum of NPF-events, (TNPF), as a function of three

858 parameters, two of which are directly measurable at the site. With the linear combination of

859 the solar flux, (SFL, Wm^{-2}), average sea surface temperature under back trajectories 36 to 48

860 hours before their arrival at the site, (T48, °C), and condensation sink, (CS, 10^5 s^{-1}):

861

862 $$TNPF = 0.57 \cdot SFL + 15.4 \cdot T48 - 0.69 \cdot CS$$

863

864 TNPF as shown in Fig. 10, can be described within an average deviation of 5% taken over the

865 major months with new particle formation, April - October. Any other of the sea surface

866 parameters describes TNPF less satisfactorily.

867

868

869

870

871 **4.3   Diurnal variability**

872

873 Average hourly occurrence of the three types of NPF-events is plotted in Fig. 11, (top). The

874 three approaches yield rather similar diel variations. From their minimum during the night

875 and early morning hours they reach their maximum occurrence between 12 and 16 h UTC in

876 the afternoon. One might expect the differences between the NPF-types to be due to the

877 requirement of the three types of NPF formation being mutually exclusive. However, this

878 constraint does not exclude that they occur at the same time of day, only that they occur at the

879 same time on the same day.

880 Over the continents new particle formation and growth events of the classical "Banana-

881 type" usually exhibit an increase in measurable precursors such as sulfuric acid shortly after

882 sunrise followed by the detection of increased numbers of nanometer-sized particles between

883 one and two hours later (Kulmala et al., 2004), who deduce a connection to photochemically

884 produced condensable vapors from this daily pattern. In the Svalbard region the sun is up all

885 day between mid-April and the end of August. Consequently we would expect the

886 photochemical production of condensable vapors to have a smaller diurnal amplitude than at

887 lower latitudes, which in turn should even out the diurnal pattern of NPF-events to some

888 degree. Despite the relatively small daily variations in solar elevations the solar flux on Mt.

889 Zeppelin varied on average by more than a factor of five during the sunlit days (see curve

890 SFL in Fig. 11, bottom). The daily maximum of SFL between 12 and 15 UTC coincides well

891 with the average diel change in N25 and NPF-occurrence. As expected in particle growth due

892 to condensable vapors after initial nucleation the daily maximum in N10 precedes that of N25

893 by a few hours.

894 The other process controlling the development of newly formed small particles is the

895 diurnal development of the planetary boundary layer, (Kulmala et al., 2004). We have no

896 data on the daily variation in boundary layer structure over or near the measurement site. The

897 ceilometer data yield the only high-resolution information with some connection to the

898 structure of the planetary boundary layer. During the summer months these data show a

899 consistent daily variation with a jump in most frequent hourly cloud base by about 100 m

900 from about 1570 m after 09 UTC with rather stable values following until 16 UTC, after

901 which cloud base decreases again to values comparable to the early morning hours. The

902 hourly medians of the vertical displacement parameter DZ, (see Fig. 11, bottom), provide a

903   clearer diurnal variation. While being negative throughout the day, i.e. indicating subsiding

904   air during the last hour before arrival at Mt. Zeppelin, DZ indicates the weakest subsidence in

905   early afternoon. We interpret diurnal variation in cloud base and DZ as indicative of local

906   clearing and convection during the day that may be conducive to photochemical processes

907   and mixing in the boundary layer, both of which would be enhancing new particle formation.

908

909

910   **5. Summary and conclusions**

911

912   Three different types of events of new particle formation, (NPF), were identified through

913   objective search algorithms formulated for the present study. The first and simplest algorithm

914   utilizes short-term increases in particle concentrations below 25 nm, (PCT-events). The

915   second one builds on the growth of the sub-50 nm diameter-median, (DGR-events), and is

916   most closely related to the classical "banana-type" of events, (Kulmala et al., 2004) involving

917   the presence of photochemically generated DMS oxidation precursors. The third and most

918   complex, so-called multiple-size approach to identifying NPF-events builds on the hypothesis

919   of Leck and Bigg (2010), suggesting the concurrent production of polymer gel particles at

920   several sizes below about 60 nm, (MEV-events).

921   With these algorithms NPF-events were identified in a ten-year record of hourly number-

922   size distributions taken at the research station on Mt. Zeppelin, Spitsbergen. As a first and

923   general conclusion we can state that NPF-events are a summer phenomenon and not related to

924   Arctic haze, which is a late winter-to-early spring event. The seasonal distribution of the

925   available information on cloudiness does not suggest any direct connection with NPF-

926   formation. The MODIS derived cloud fraction generally is very high (70 – 90%) and rather

927   evenly distributed over the Svalbard region during the months with high frequencies of NPF-

928   events. As already reported in Tunved et al. (2013) NPF-events appear to be somewhat

929 sensitive to the available data on precipitation derived from the trajectory model, in particular

930 when constrained to cases with back trajectories staying below 500 m. In this subpopulation

931 of NPF-events DGR-events show the strongest change in precipitation parameters in

932 connection with new particle formation.

933   The seasonal distribution of solar flux suggests some photochemical control that may

934 affect marine biological processes generating particle precursors and/or atmospheric

935 photochemical processes that generate condensable vapors from precursor gases. Whereas

936 the seasonal distribution of the biogenic MSA follows that of the solar flux it peaks before the

937 maxima in NPF-occurrence. For PCT-events, and more distinctly so for DGR-events, this

938 one-month delay disappears in the subpopulation with back trajectories staying below 500 m.

939 MEV-events, however, maintain their peak occurrence later in summer and early fall.

940   With the limited information on particle size, composition, particle precursors, and

941 environmental conditions no definitive statements can be made about the processes leading to

942 the formation of new particles in the Svalbard region. A host of findings, however, point to

943 varying and rather complex marine biological source processes. The potential source regions

944 for all types of new particle formation appear to be restricted to the marginal ice and open

945 water areas between Northeastern Greenland and Eastern Svalbard. During earliest and latest

946 months with high numbers of NPF-events the back trajectories reach farther south into the

947 open waters of the North Atlantic. Depending on conditions yet to be clarified new particle

948 formation may become visible as short bursts of particles around 20 nm, (PCT-events), longer

949 events involving condensation growth, (DGR-events), or extended events with elevated

950 concentrations of particles at several sizes below 100 nm, (MEV-events). The seasonal

951 distribution of NPF-events peaks later than that of MSA and, DGR and in particular of MEV-

952 events reach into late summer and early fall with much open, warm, and DMSPt-rich waters

953 around Svalbard, promoting the production of *Phaeocystis pouchetii* together with polymer

954 gels. Consequently, a simple model to describe the seasonal distribution of the total number

of NPF-events can be based on solar flux, and sea surface temperature, representing environmental conditions for marine biological activity, and condensation sink, controlling the balance between new particle nucleation and their condensational growth. Based on the sparse knowledge about the seasonal cycle of gel-forming marine microorganisms and their controlling factors we hypothesize that the seasonal distribution of DGR and more so MEV-events reflect the seasonal cycle of the gel-forming phytoplankton.

Despite the rather small diel changes expected during the summer Arctic there is a significant diurnal variation in aerosol and environmental parameters. Diurnal distributions of particle numbers below ten, (N10), and below 25 nm, (N25) follow that of the solar flux rather closely with a maximum between 14 and 16 UTC with the maximum of N10 occurring a few hours before that of N25. This delay in maxima may be caused by a slow particle growth due to photochemically produced condensable vapors. With a peak around noon MEV-events show the earliest daily peak occurrence with PCT and DGR-events peaking between 15 and 17 h, more closely to the maximum solar flux. Considering the diurnal variation in vertical trajectory displacement, (DZ), the early daily maximum in MEV-occurrence may be simply controlled by boundary layer dynamics.

With the large database of ten years of aerosol data on Mt. Zeppelin enriched by environmental atmospheric and marine data occurrences, pathways and potential source areas of different types of new particle formation in the Svalbard region were elucidated by the present study. More process related information about new particle formation would require dedicated mechanistic experiments with more detailed information on particle precursors, ultrafine particles, and boundary layer mixing processes. DGR and MEV-types of new particle formation seem to be more closely related to near-surface processes. Thus, a low-level site such as the reopened Station Nord, (Nguyen et al., 2016), would be more suitable for related mechanistic experiments. Station Nord has the additional advantage of being close to the potential source regions of DGR and MEV-events identified by the present study.

1000

1001 Agarwal, J. K., and Sem, G. J.: Continuous flow, single-particle-counting condensation nucleus counter, J. Aerosol Sci., 11, 343-357, 1980.

1003 An, N., and Wang, K.: A Comparison of MODIS-Derived Cloud Fraction with Surface Observations at Five SURFRAD Sites, J. Appl. Meteor. Clim., 54, 1009-1020, 2015.

1005 Asmi, E., Kondratyev, V., Brus, D., Laurila, T., Lihavainen, H., Backman, J., Vakkari, V., Aurela, M., Hatakka, J., Viisanen, Y., Uttal, T., Ivakhov, V., and Makshtas, A.: Aerosol size distribution seasonal characteristics measured in Tiksi, Russian Arctic, Atmos. Chem. Phys., 16, 1271-1287, 10.5194/acp-16-1271-2016, 2016.

1009 Ayers, G. P., Cainey, J. M., Granek, H., and Leck, C.: Dimethylsulfide oxidation and the ratio of methansulfonate to non sea-salt sulfate in the marine aerosol, J. Atmos. Chem., 25, 307-325, 1996.

1012 Bates, T. S., Johnson, J. E., Quinn, P. K., Goldan, P. D., Kuster, W. C., Covert, D. C., and Hahn, C. J.: The biogeochemical sulfur cycle in the marine boundary layer over the Northeast Pacific Ocean, J. Atmos. Chem., 10, 59-81, 1990.

1015 Becagli, S., Lazzara, L., Marchese, C., Dayan, U., Ascanius, S. E., Cacciani, M., Caiazzo, L., Di Biagio, C., Di Iorio, T., di Sarra, A., Eriksen, P., Fani, F., Giardi, F., Meloni, D., Muscari, G., Pace, G., Severi, M., Traversi, R., and Udisti, R.: Relationships linking primary production, sea ice melting, and biogenic aerosol in the Arctic, Atmos. Environ., 136, 1-15, http://dx.doi.org/10.1016/j.atmosenv.2016.04.002, 2016.

1020 Beine, H. J., Argentini, S., Maurizi, A., Mastrantonio, G., and Viola, A.: The local wind field at Ny-Ålesund and the Zeppelin mountain at Svalbard, Meteorol. Atmos. Phys., 78, 107–113, 2001.

1023 Bélanger, S., Babin, M., and Tremblay, J.-É.: Increasing cloudiness in Arctic damps the increase in phytoplankton primary production due to sea ice receding, Biogeosciences, doi:10.5194/bg-5110-4087-2013, 2013.

1026 Blanchard, D. C., and Woodcock, A. H.: Bubble formation and modification in the sea and its meteorological significance, Tellus, 9, 145-158, 1957.

1028 Browse, J., Carslaw, K. S., Mann, G. W., Birch, C. E., Arnold, S. R., and Leck, C.: The complex response of Arctic aerosol to sea-ice retreat, Atmos. Chem. Phys., 14, 7543-7557, 10.5194/acp-14-7543-2014, 2014.

1031 Charlson, R. J., Lovelock, J. E., Andreae, M. O., and Warren, S. G.: Oceanic phytoplankton, atmospheric sulphur, cloud albedo and climate, Nature, 326, 655-661, 1987.

1033 Croft, B., Martin, R. V., Leaitch, W. R., Tunved, P., Breider, T. J., D'Andrea, S. D., and
1034   Pierce, J. R.: Processes controlling the annual cycle of Arctic aerosol number and size
1035   distributions, Atmos. Chem. Phys., 16, 3665-3682, 10.5194/acp-16-3665-2016, 2016a.

1036 Croft, B., Wentworth, G. R., Martin, R. V., Leaitch, W. R., Murphy, J. G., Murphy, B. N.,
1037   Kodros, J. K., Abbatt, J. P. D., and Pierce, J. R.: Contribution of Arctic seabird-colony
1038   ammonia to atmospheric particles and cloud-albedo radiative effect, Nature
1039   Communications, 7, 13444, 10.1038/ncomms13444

1040 http://www.nature.com/articles/ncomms13444 - supplementary-information, 2016b.

1041 Dal Maso, M., Kulmala, M., Riipinen, I., Wagner, R., Hussein, T., Aalto, P. P., and Lehtinen,
1042   K. E. J.: Formation and growth of fresh atmospheric aerosols: eight years of aerosol
1043   size distribution data from SMEAR II, Hyytiälä, Finland, Bor. Env. Res., 10, 323-336,
1044   2005.

1045 Das, R., Granat, L., Leck, C., Praveen, P. S., and Rodhe, H.: Chemical composition of
1046   rainwater at Maldives Climate Observatory at Hanimaadhoo (MCOH), Atmos. Chem.
1047   Phys., 11, 3743-3755, 10.5194/acp-11-3743-2011, 2011.

1048 Dee, D. P., Uppala, S. M., Simmons, A. J., Berrisford, P., Poli, P., Kobayashi, S., and
1049   Bechtold, P.: The ERA‑Interim reanalysis: Configuration and performance of the
1050   data assimilation system, Q. J. Roy. Meteorol. Soc., 137, 553-597, 2011.

1051 Draxler, R., and Rolph, G.: HYSPLIT (HYbrid Single-Particle Lagrangian Integrated
1052   Trajectory) Model access via NOAA ARL READY, NOAA Air Resources
1053   Laboratory, Silver Spring, MD, 2003.

1054 Ehn, M., Vuollekoski, H., Petäjä, T., Kerminen, V.-M., Vana, M., Aalto, P., de Leeuw, G.,
1055   Ceburnis, D., Dupuy, R., O'Dowd, C. D., and Kulmala, M.: Growth rates during
1056   coastal and marine new particle formation in western Ireland, J. Geophys. Res., 115,
1057   n/a-n/a, 10.1029/2010JD014292, 2010.

1058 Flyger, H., and Heidam, N. Z.: Ground level measurements of the summer tropospheric
1059   aerosol in Northern Greenland, J. Aerosol Sci., 9, 157-168, 1978.

1060 Galí, M., Devred, E., Levasseur, M., Royer, S.-J., and Babin, M.: A remote sensing algorithm
1061   for planktonic dimethylsulfoniopropionate (DMSP) and an analysis of global patterns,
1062   Remote Sens. Environ., 171, 171-184, http://dx.doi.org/10.1016/j.rse.2015.10.012,
1063   2015.

1064 Galí, M., and Simó, R.: A meta‑analysis of oceanic DMS and DMSP cycling processes:
1065   Disentangling the summer paradox, Global Biochem. Cycles, 29, 496-515, 2015.

1066   Gao, Q., Leck, C., Rauschenberg, C., and Matrai, P. A.: On the chemical dynamics of
1067   extracellular polysaccharides in the high Arctic surface microlayer, Ocean Sci.
1068   Discuss., 9, 215–259, 2012.

1069   Heintzenberg, J., Bischof, W., Odh, S.-Å., and Moberg, B.: An investigation of possible sites
1070   for a background monitoring station in the European Arctic., International
1071   Meteorological Institute in Stockholm, Department of Meteorology, Stockholm
1072   University, Stockholm, Report Nr. AP-22, 74 pp, 1983.

1073   Heintzenberg, J., and Larssen, S.: SO_2 and SO_4 in the Arctic: Interpretation of observations at
1074   three Norwegian Arctic-subArctic stations, Tellus, 35B, 255-265, 1983.

1075   Heintzenberg, J.: Arctic haze: air pollution in polar regions, AMBIO, 18, 50-55, 1989.

1076   Heintzenberg, J., and Leck, C.: Seasonal variation of the atmospheric aerosol near the top of
1077   the marine boundary layer over Spitsbergen related to the Arctic sulphur cycle, Tellus,
1078   46B, 52-67, 1994.

1079   Heintzenberg, J., Leck, C., Birmili, W., Wehner, B., Tjernström, M., and Wiedensohler, A.:
1080   Aerosol number-size distributions during clear and fog periods in the summer high
1081   Arctic: 1991, 1996, and 2001, Tellus, 58B, 41-50, 2006.

1082   Heintzenberg, J., Wehner, B., and Birmili, W.: "How to find bananas in the atmospheric
1083   aerosol" New approach for analyzing atmospheric nucleation and growth events,
1084   Tellus B, 59, 273-282, 2007.

1085   Heintzenberg, J.: The aerosol-cloud-climate conundrum, IJGW, 4, 219-241, 2012.

1086   Heintzenberg, J., Leck, C., and Tunved, P.: Potential source regions and processes of aerosol
1087   in the summer Arctic, Atmos. Chem. Phys., 15, 6487-6502, 10.5194/acp-15-6487-
1088   2015, 2015.

1089   Held, A., Brooks, I. M., Leck, C., and Tjernström, M.: On the potential contribution of open
1090   lead particle emissions to the central Arctic aerosol concentration, Atmos. Chem.
1091   Phys., 11, 3093-3105, 10.5194/acp-11-3093-2011, 2011a.

1092   Held, A., Orsini, D. A., Vaattovaara, P., Tjernström, M., and Leck, C.: Near-surface profiles
1093   of aerosol number concentration and temperature over the Arctic Ocean, Atmos.
1094   Meas. Tech., 4, 1603–1616, 2011b.

1095   Hubanks, P., Platnick, S., King, M., and Ridgway, B.: MODIS Atmosphere L3 Gridded
1096   Product Algorithm Theoretical Basis, Document (ATBD) and Users Guide, 2015.

1097   Huschke, R. E.: Arctic cloud statistics from "air calibrated" surface weather observations,
1098   Rand Corporation Memo. RM 6173-PR, 79 pp, 1969.

1099   IOCCG: Ocean Colour Remote Sensing in Polar Seas, Report 16, Eds. Babin, M., Arrigo, K.,
1100   Bélanger, S. and Forget, M.-H., 129 pp, 2015.

1101   Jaenicke, R., and Schütz, L.: Arctic aerosols in surface air, Időjaras, 86, 235-241, 1982.

1102   Junge, C. E.: Air chemistry and Radioactivity, Academic Press, New York and London, 382
1103   pp., 1963.

1104   Junninen, H., Hulkkonen, M., Riipinen, I., Nieminen, T., Hirsikko, A., Suni, T., Boy, M., Lee,
1105   S.-H., Vana, M., Tammet, H., Kerminen, V.-M., and Kulmala, M.: Observations on
1106   nocturnal growth of atmospheric clusters, Tellus B, 60, 365-371, 2008.

1107   Karl, M., Gross, A., Leck, C., and Pirjola, L.: Intercomparison of dimethylsulfide oxidation
1108   mechanisms for the marine boundary layer: Gaseous and particulate sulfur
1109   constituents, J. Geophys. Res., 112, D15304, 10.1029/2006JD007914, 2007.

1110   Karl, M., Leck, C., Gross, A., and Pirjola, L.: A Study of New Particle Formation in the
1111   Marine Boundary Layer Over the Central Arctic Ocean using a Flexible
1112   Multicomponent Aerosol Dynamic Model, Tellus, 64B,
1113   doi:http://dx.doi.org/10.3402/tellusb.v3464i3400.17158, 2012.

1114   Karl, M., Leck, C., Coz, E., and Heintzenberg, J.: Marine nanogels as a source of atmospheric
1115   nanoparticles in the high Arctic, Geophys. Res. Lett., 40, 3738–3743, DOI:
1116   10.1002/grl.50661, 2013.

1117   Keene, W. C., Pszenny, A. A. P., Galloway, J. N., and Hawley, M. E.: Sea-salt corrections
1118   and interpretation of constituent ratios in marine precipitation, J. Geophys. Res., 91,
1119   6647-6658, 1986.

1120   Keller, M. D., Bellows, W. K., and Guillard, R. R. L.: A survey of dimethylsulfide production
1121   in 12 classes of marine phytoplankton, in: Biogenic sulfur in the environment, edited
1122   by: E.S. Saltzman, and Cooper, W. J., American Chemical Society, Washington, D,
1123   167–182, 1989.

1124   King, M. D., Platnick, S., Menzel, W. P., Ackerman, S. A., and Hubanks, P. A.: Spatial and
1125   temporal distribution of clouds observed by MODIS onboard the Terra and Aqua
1126   satellites, IEEE Trans. Geosci. Remote Sens., 51, 3826–3852, 2013.

1127   Knutson, E. O., and Whitby, K. T.: Accurate Measurement of Aerosol Electrical Mobility
1128   Moments, J. Aerosol Sci., 6, 453-460, 1975a.

1129   Knutson, E. O., and Whitby, K. T.: Aerosol classification by electric mobility: apparatus,
1130   theory, and applications, J. Aerosol Sci., 6, 443-451, 1975b.

1131 Kulmala, M., Dal Maso, M., Mäkelä, J. M., Pirjola, L., Väkevä, M., Aalto, P. P.,
1132   Miikkulainen, P., Hämeri, K., and O'Dowd, C. D.: On the formation, growth and
1133   composition of nucleation mode particles, Tellus, 53B, 479-490, 2001.

1134 Kulmala, M., Vehkamäkia, H., Petäjä, T., Dal Maso, M., Lauri, A., Kerminen, V.-M., Birmili,
1135   W., and McMurry, P. H.: Formation and growth rates of ultrafine atmospheric
1136   particles: a review of observations, J. Aerosol Sci., 35, 143-176, 2004.

1137 Lana, A., Simó, R., Vallina, S. M., and Dachs, J.: Re-examination of global emerging patterns
1138   of ocean DMS concentration, Biogeochem., 110, 173-182, 2012.

1139 Lannefors, H., Heintzenberg, J., and Hansson, H.-C.: A comprehensive study of physical and
1140   chemical parameters of the Arctic summer aerosol; results from the Swedish
1141   expedition Ymer-80, Tellus, 35B, 40-54, 1983.

1142 Leck, C., and Persson, C.: The central Arctic Ocean as a source of dimethyl sulfide: Seasonal
1143   variability in relation to biological activity, Tellus, 48B, 156-177, 1996a.

1144 Leck, C., and Persson, C.: Seasonal and short-term variability in dimethyl sulfide, sulfur
1145   dioxide and biogenic sulfur and sea salt aerosol particles in the arctic marine boundary
1146   layer, during summer and autumn, Tellus, 48B, 272-299, 1996b.

1147 Leck, C., and Bigg, E. K.: Aerosol production over remote marine areas - A new route,
1148   Geophys. Res. Lett., 23, 3577-3581, 1999.

1149 Leck, C., and Bigg, E. K.: New particle formation of marine biological origin, Aerosol Sci.
1150   Technol., 44, 570-577, 2010.

1151 Leck, C., Gao, Q., Mashayekhy Rad, F., and Nilsson, U.: Size-resolved atmospheric
1152   particulate polysaccharides in the high summer Arctic, Atmos. Chem. Phys., 13,
1153   12573-12588, 10.5194/acp-13-12573-2013, 2013.

1154 Lindsay, R., Wensnahan, M., Schweiger, A., and Zhang, J.: Evaluation of seven different
1155   atmospheric reanalysis products in the Arctic, J. Clim., 27, 2588-2606, 2014.

1156 Liss, P. S., and Merlivat, L.: Air-sea gas exchange rates: Introduction and synthesis, in: The
1157   Role of Air-Sea Exchange in Geochemical Cycling, edited by: Buat-Menard, P.,
1158   Reidel, Norwell, MS, 113-127, 1986.

1159 Maritorena, S., Siegel, D. A., and Peterson, A. R.: Optimization of a semianalytical ocean
1160   color model for global-scale applications, Appl. Opt., 41.15, 2705-2714, 2002.

1161 Matrai, P. A., and Vernet, M.: Dynamics of the vernal bloom in the marginal ice zone of the
1162   Barents Sea: Dimethyl sulfide and dimethylsulfoniopropionate budgets, Journal of
1163   Geophysical Research: Oceans, 102, 22965-22979, 10.1029/96JC03870, 1997.

Nguyen, Q. T., Glasius, M., Sørensen, L. L., Jensen, B., Skov, H., Birmili, W., Wiedensohler, A., Kristensson, A., Nøjgaard, J. K., and Massling, A.: Seasonal variation of atmospheric particle number concentrations, new particle formation and atmospheric oxidation capacity at the high Arctic site Villum Research Station, Station Nord, Atmos. Chem. Phys., 16, 11319–11336, 10.5194/acp-2016-205, 2016.

Norman, A. L., Barrie, L. A., Toom-Sauntry, D., Sirois, A., Krouse, H. R., Li, S. M., and Sharma, S.: Sources of aerosol sulphate at Alert: Apportionment using stable isotopes, J. Geophys. Res., 104, 11619-11631, 1999.

O'Dowd, C., Monahan, C., and Dall'Osto, M.: On the occurrence of open ocean particle production and growth events, Geophys. Res. Lett., 37, L19805, doi:19810.11029/12010GL044679, 2010.

Orellana, M. V., Matrai, P. A., Janer, M., and Rauschenberg, C. D.: Dimethylsulfoniopropionate storage in *Phaecystis* (Prymnesiophyceae) secretory vesicles J. Phycol., 47, 112-117, 10.1111/j.1529-8817.2010.00936.x, 2011a.

Orellana, M. V., Matrai, P. A., Leck, C., Rauschenberg, C. D., Lee, A. M., and Coz, E.: Marine microgels as a source of cloud condensation nuclei in the high Arctic, PNAS, 108, 13612–13617, 2011b.

Pirjola, L., Kulmala, M., Wilck, M., Bischoff, A., Stratmann, F., and Otto, E.: Formation of sulphuric acid aerosols and cloud condensation nuclei: An expression for significant nucleation and model comparison, J. Aerosol Sci., 30, 1079-1094, 1999.

Polissar, A. V., Hopke, P. K., Paatero, P., Kaufman, Y. J., Hall, D. K., Bodhaine, B. A., Dutton, E. G., and Harris, J. M.: The aerosol at Barrow, Alaska: long-term trends and source locations, Atmos. Environ., 33, 2441-2458, 1999.

Rahn, K. A., and Shaw, G. E.: Particulate air pollution in the Arctic: Large-scale occurence and meteorological controls, in: Atmospheric Aerosols and Nuclei, edited by: Roddy, F., and O'Connor, T. C., Dept. of Physics, University College, Galway, Ireland 21-27 Sept., 223-227, 1977.

Ristovski, Z. D., Suni, T., Kulmala, M., Boy, M., Meyer, N. K., Duplissy, J., Turnipseed, A., Morawska, L., and Baltensperger, U.: The role of sulphates and organic vapours in growth of newly formed particles in a eucalypt forest, Atmos. Chem. Phys., 10, 2919-2926, 10.5194/acp-10-2919-2010, 2010.

Rudels, B., Björk, G., Nilsson, J., Winsor, P., Lake, I., and Nohr, C.: The interaction between waters from the Arctic Ocean and the Nordic Seas north of Fram Strait and along the

1197   East Greenland Current: results from the Arctic Ocean-02 Oden expedition, Journal of
1198   Marine Systems, 55, 1-30, 2005.

1199 Schmidtko, S., Johnson, G. C., and Lyman, J. M.: MIMOC: A global monthly isopycnal
1200   upper-ocean climatology with mixed layers, Journal of Geophysical Research:
1201   Oceans, 118, 1658-1672, 10.1002/jgrc.20122, 2013.

1202 Schoemann, V., Becquevort, S., Stefels, J., Rousseau, V., and Lancelot, C.: Phaeocystis
1203   blooms in the global ocean and their controlling mechanisms: a review, Journal of Sea
1204   Research, 53, 43-66, http://dx.doi.org/10.1016/j.seares.2004.01.008, 2005.

1205 Sharma, S., Chan, E., Ishizawa, M., Toom-Sauntry, D., Gong, S. L., Li, S. M., Tarasick, D.
1206   W., Leaitch, W. R., Norman, A., Quinn, P. K., Bates, T. S., Levasseur, M., Barrie, L.
1207   A., and Maenhaut, W.: Influence of transport and ocean ice extent on biogenic aerosol
1208   sulfur in the Arctic atmosphere, J. Geophys. Res., 117, D12209,
1209   10.1029/2011JD017074, 2012.

1210 Simó, R.: Production of atmospheric sulfur by oceanic plankton: biogeochemical, ecological
1211   and evolutionary links, Trends in Ecology & Evolution, 16, 287-294, 2001.

1212 Stohl, A.: Computations, accuracy and applications of trajectories - A review and
1213   bibliography, Atmos. Environ., 32, 947-966, 1998.

1214 Ström, J., Engvall, A.-C., Delbart, F., Krejci, R., and Treffeisen, R.: On small particles in the
1215   Arctic summer boundary layer: observations at two different heights near Ny-Ålesund,
1216   Svalbard, Tellus B - Chemical and Physical Meteorology, 61, 473-482, 2009.

1217 Suni, T., Kulmala, M., Hirsikko, A., Bergman, T., Laakso, L., Aalto, P. P., Leuning, R.,
1218   Cleugh, H., Zegelin, S., Hughes, D., van Gorsel, E., Kitchen, M., Vana, M., Hõrrak,
1219   U., Mirme, S., Mirme, A., Sevanto, S., Twining, J., and Tadros, C.: Formation and
1220   characteristics of ions and charged aerosol particles in a native Australian Eucalypt
1221   forest, Atmos. Chem. Phys., 8, 129-139, 10.5194/acp-8-129-2008, 2008.

1222 Tunved, P., Ström, J., and Krejci, R.: Arctic aerosol life cycle: linking aerosol size
1223   distributions observed between 2000 and 2010 with air mass transport and
1224   precipitation at Zeppelin station, Ny-Ålesund, Svalbard, Atmos. Chem. Phys., 13,
1225   3643–3660, 10.5194/acpd-12-29967-2012, 2013.

1226 Warren, S. G., and Hahn, C. J.: Cloud climatology, in: Encyclopedia of Atmospheric
1227   Sciences, edited by: Holton, J. R., Pyle, J., and Curry, J. A., Academic Press, London,
1228   UK, 476-483, 2002.

1229 Wiedensohler, A., Covert, D., Swietlicki, E., Aalto, P., Heintzenberg, J., and Leck, C.:
1230   Occurrence of an ultrafine particle mode less than 20 nm in diameter in the marine
1231   boundary layer of the Arctic summer and autumn, Tellus, 48B, 213-222, 1996.

1232 Willis, M. D., Burkart, J., Thomas, J. L., Köllner, F., Schneider, J., Bozem, H., Hoor, P. M.,
1233   Aliabadi, A. A., Schulz, H., Herber, A. B., Leaitch, W. R., and Abbatt, J. P. D.:
1234   Growth of nucleation mode particles in the summertime Arctic: a case study, Atmos.
1235   Chem. Phys. Discuss., 2016, 1-31, 10.5194/acp-2016-256, 2016.

1236 Zhang, M., Chen, L., Xu, G., Lin, Q., and Liang, M.: Linking Phytoplankton Activity in
1237   Polynyas and Sulfur Aerosols over Zhongshan Station, East Antarctica, J. Atmos. Sci.,
1238   72, 4629-4642, 2015.

1239

1240

1241

1242

Parameter	TR (h)	Explanation
C25	1 min	25% percentile of cloud base from AWI ceilometer (m)
CF12, 24, 36, 48, 5D	24	Average MODIS cloud fraction during the last 12h, 24h, 36, 48h, and days 3-5 before trajectory arrival
D50	1	Number-median diameter of particles < 50 nm diameter
CS	1	Condensation sink (s^{-1})
DZ	1	Vertical trajectory displacement $(m\ h^{-1})$ during the last hour before arrival
MSA	≥1 day	Methane sulfonate $(nmolm^{-3})$
N10	1	Number concentration of particles up to 10 nm $(>2010, cm^{-3})$
N20	1	Number concentration between 10 and 20 nm (cm^{-3})
N25	1	Number concentration of particles up to 25 nm (cm^{-3})
N40	1	Number concentration between 20 and 40 nm (cm^{-3})
N60	1	Number concentration between 40 and 60 nm (cm^{-3})
N100	1	Number concentration between 60 and 100 nm (cm^{-3})
N300	1	Number concentration between 100 and 300 nm (cm^{-3})
Na	≥1 day	Sodium concentrations $(nmolm^{-3})$
NCO	1	Number concentration of particles > 300 nm (cm^{-3})
$nssSO_4^{2-}$	≥1 day	Non-sea salt sulfate concentrations $(nmolm^{-3})$
NTO	1	Number concentration of particles ≥ 10 nm, $cm^{-3})$
OC12, 24, 36, 48, 5D	120	Average MODIS DMSPt (nmol) during the last 12h, 24h, 36, 48h, and days 3-5 before trajectory arrival
OW12, 24, 36, 48, 5D	24	Average open water (%) during the last 12h, 24h, 36, 48h, and days 3-5 before trajectory arrival
PRE	1	Trajectory precipitation (mm) at arrival
RH	1	Trajectory relative humidity (%) at arrival
SFL	1	Solar flux at trajectory arrival (Wm^{-2})
SP12, 24, 36, 48, 5D	1	Accumulated precipitation (mm) during the last 12h, 24h, 36, 48h, and days 3-5 before trajectory arrival
T12, 24, 36, 48, 5D	24	Average sea surface temperature (C) during the last 12h, 24h, 36, 48h, and days 3-5 before trajectory arrival
TEM	1	Trajectory temperature (C) at arrival
WDR	1	Trajectory wind direction (°) during the last hour before arrival
WSP	1	Trajectory wind speed $(m\ sec^{-1})$ during the last hour before arrival

1243

1244   Table 1 Aerosol, atmospheric, and ocean parameters utilized in the present study.

1245   DMSPt = Total dimethylsulfoniopropionate in surface ocean waters. TR = temporal

1246   resolution in which the respective data were available. All parameter explanations

1247   starting with "Trajectory" refer to parameters calculated by HYSPLIT4 at each
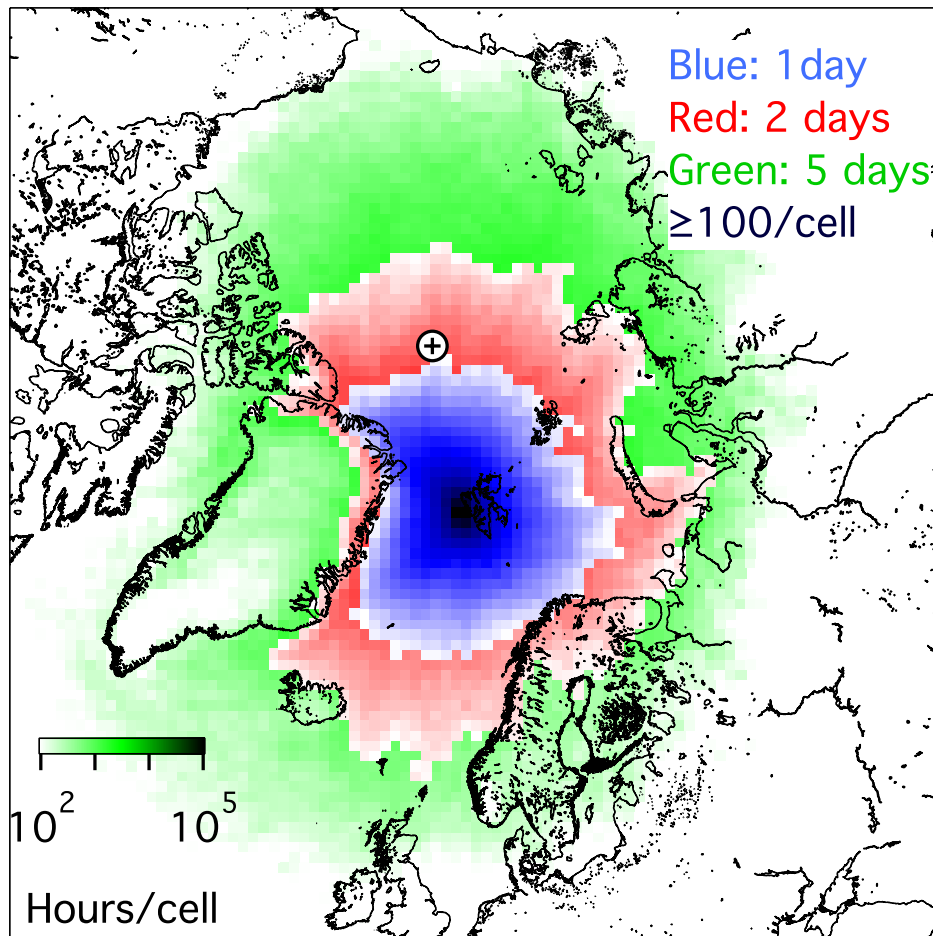
1248   trajectory step.

1249

1250

1251

1252

1253

1254

1255

1256

1257

Approach	Acronym	Criteria and thresholds	Total number of events	Number of unique events	% of total number of data hours
Percentiles	PCT	N25 >93%-percentile	4143	240	1
Diameter-growth	DGR	D50-Growth >1.5	1199	235	3
Multi-size growth	MEV	Multi-growth >1.6	1191	266	4
Sum			6533	741	

1258

1259   Table 2 Total and unique number of events of new particle formation identified by the three

1260   approaches to identify NPF-events, and percent of all data hours covered by unique

1261   events.

1262

Blue: 1day
Red: 2 days
Green: 5 days
≥100/cell

10^2 10^5
Hours/cell

1263

1264   Fig. 1   Map of the regional distribution of 5-day (green), 2-day (red), and 1-day (blue)

1265   hourly back trajectories to Mt. Zeppelin during the months March through October

1266   of the years 2006 - 2015. Black symbol: North Pole. The colored areas are covered

1267   with at least 100 trajectory hours per geocell and the color saturation corresponds to

1268   the number of trajectory hours per grid cell on a log-scale.

1269
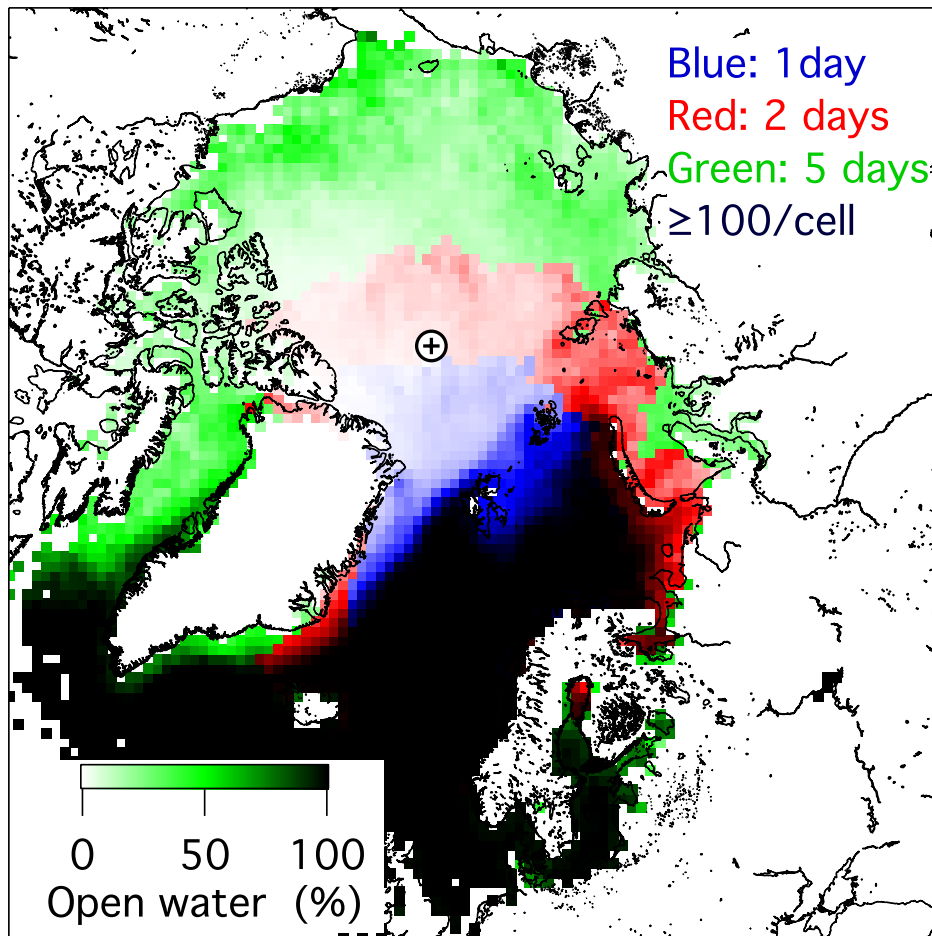
1270

1271   Fig. 2   Map of the regional distribution of open water under 87648 5-day (green), 2-day

1272   (red), and 1-day (blue) hourly back trajectories to Mt. Zeppelin during the during the

1273   months March through October of the years 2006-2015. Black symbol: North Pole.

1274   The areas are covered with at least 100 trajectory hours concurrent with data values

1275   per geocell.

1276
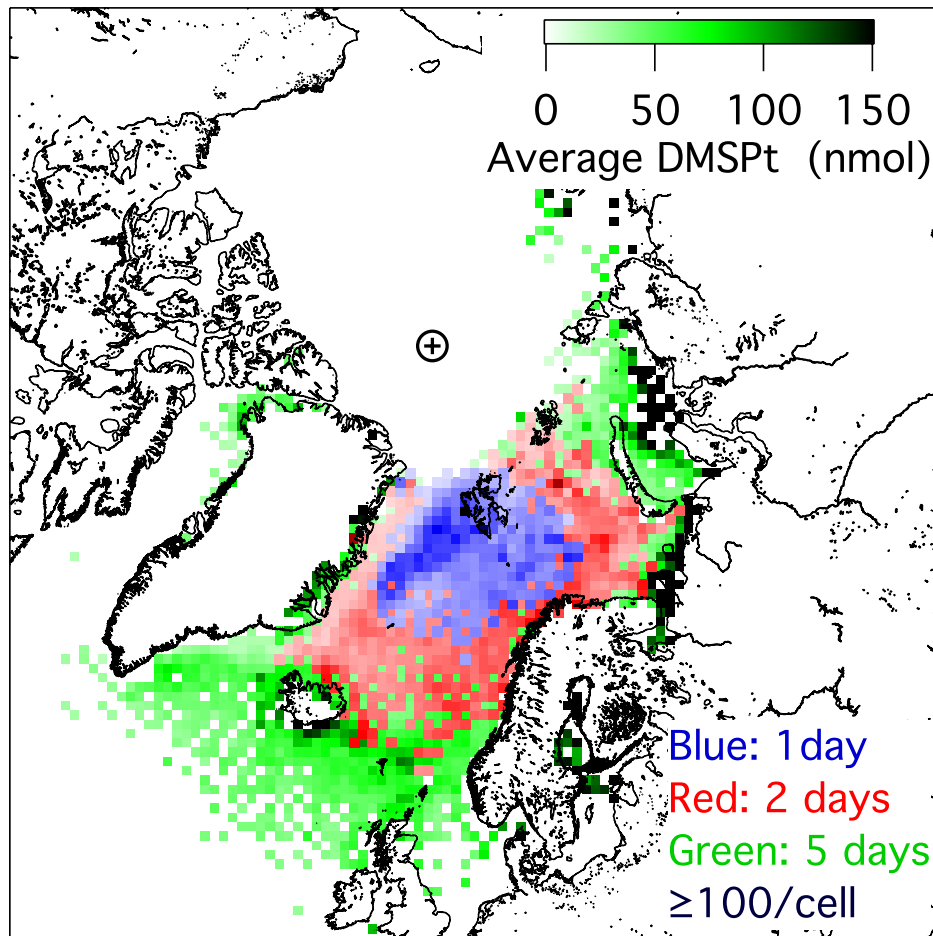
1277

1278   Fig. 3   Map of the regional distribution of DMSPt along 87648 5-day (green), 2-day (red),

1279   and 1-day (blue) hourly back trajectories to Mt. Zeppelin during the during the

1280   months March through October of the years 2006-2015. Black symbol: North Pole.

1281   The relative color scale holds for all colors. The areas are covered with at least 100

1282   trajectory hours with data values per geocell.

1283
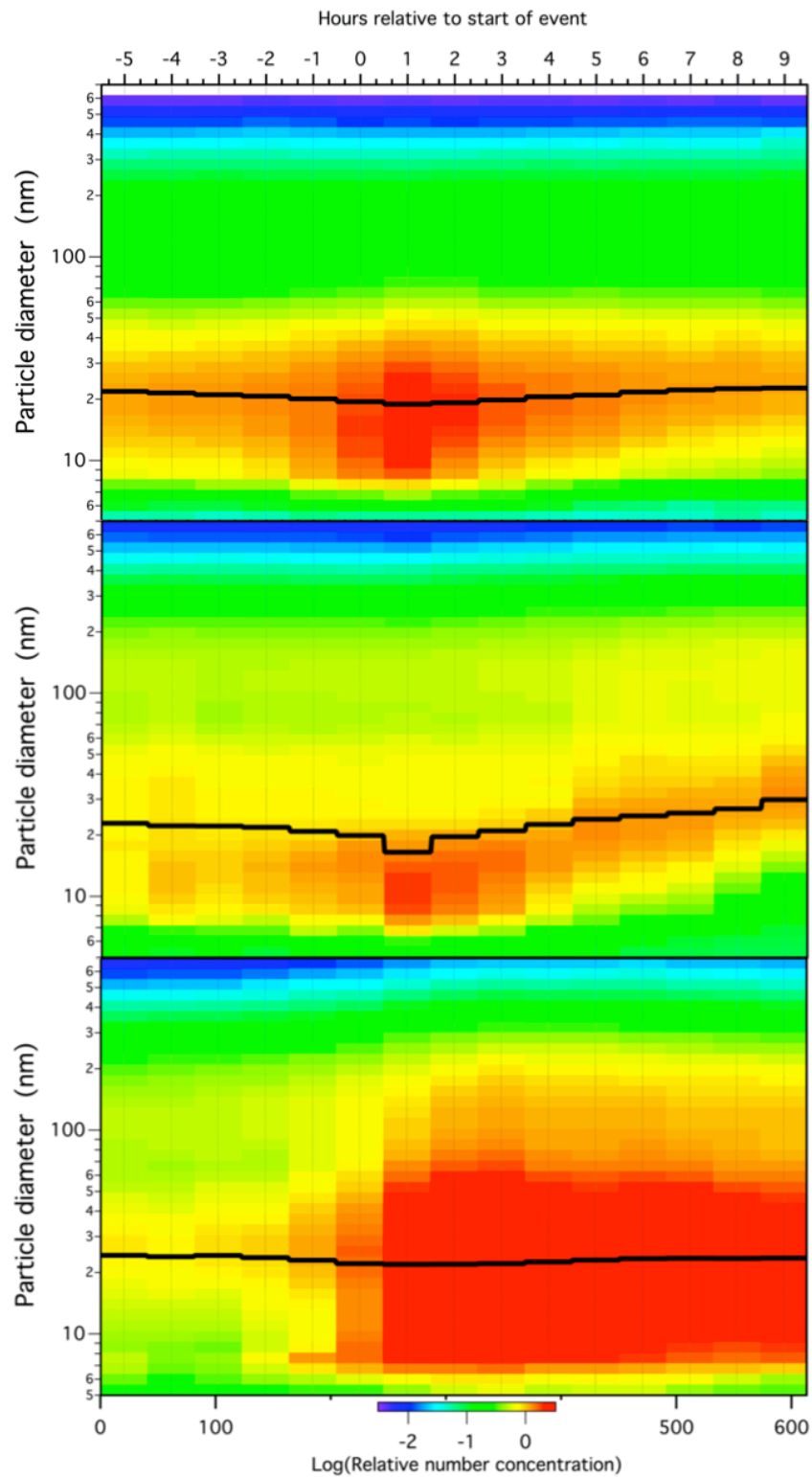
1284

1285   Fig.4   Average temporal development of the relative number size distribution before and

1286   during NPF-events identified by the three approaches. The black curve gives the

1287   median sub-50-nm particle diameter D50 during the events. Top: PCT-events;

1288   center: DGR-events; bottom: MEV-events.

1289
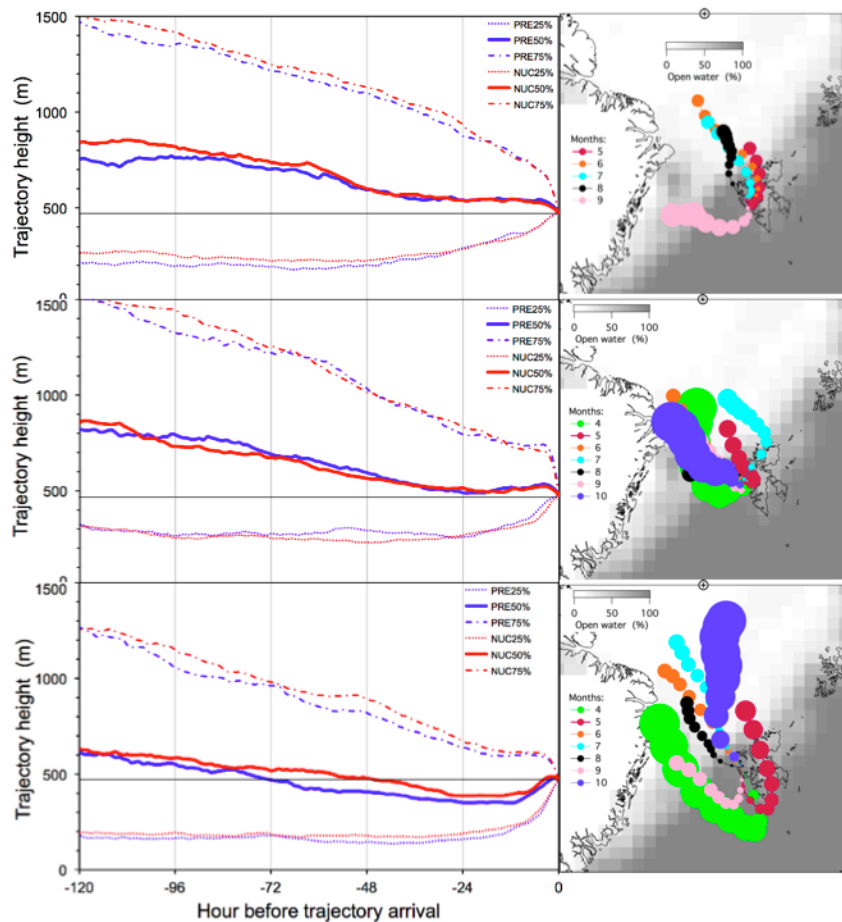
1290

1291   Fig. 5   Left panels: Median back trajectory height profiles (m) during the six pre-event

1292   hours (full line in blue, PRENUC) and during the nine DGR-event hours (full line in

1293   red, NUC). 25% and 75% percentiles are shown as dotted, and dash-dotted lines,

1294   respectively. Top: PCT-events; center: DGR-events; bottom: MEV-events. The thin

1295   horizontal line marks the station level.

1296   Right panels: Average monthly trajectory positions in 12 h steps for the months April

1297   though October. Only months with at least 10 NPF-events are shown. The circles

1298   comprise 95% of all trajectories at any trajectory step. The underlying grey-scale

1299   map indicates July ice cover averaged over the years 2006 – 2015

1300
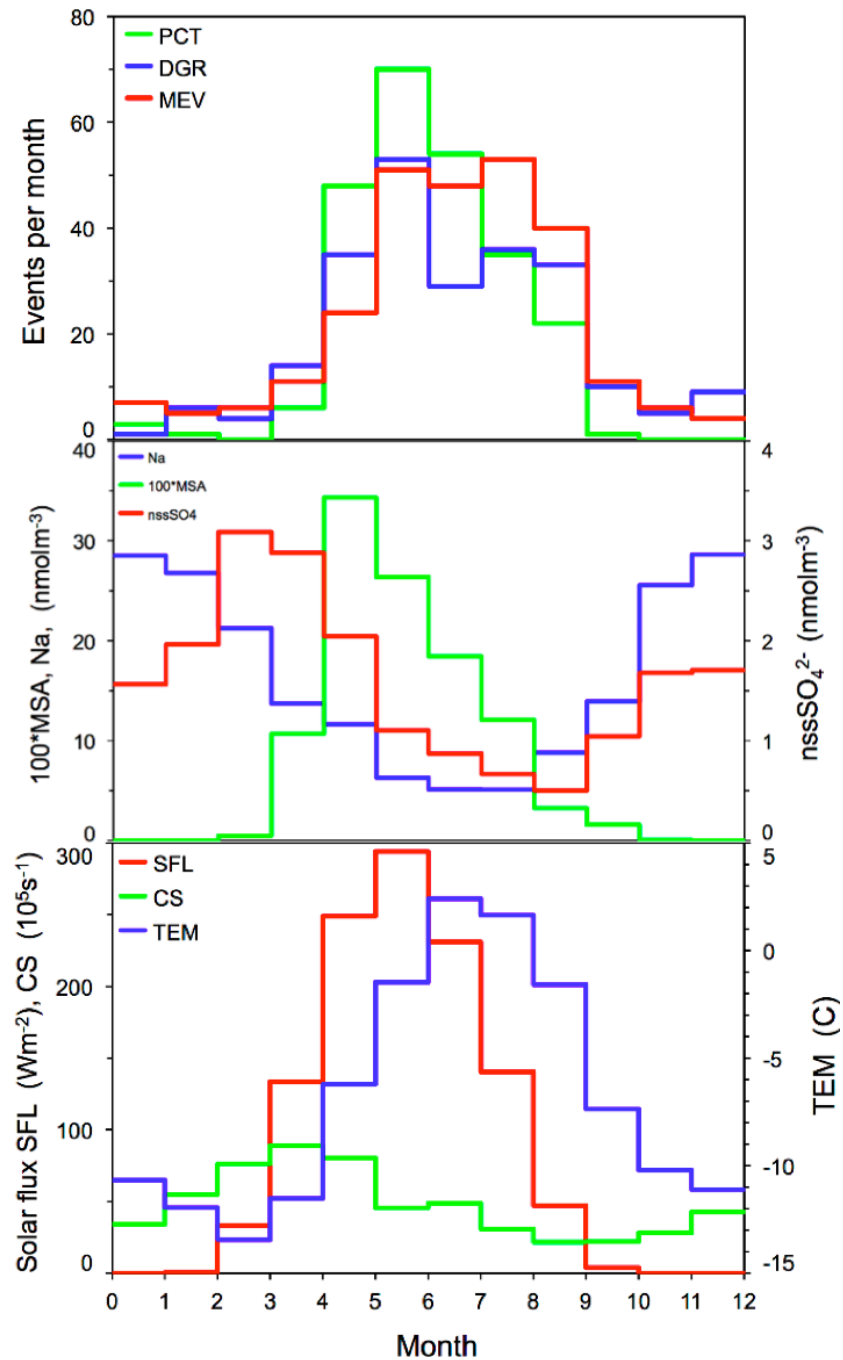
1301

Fig. 6   Top: Monthly numbers of new particle formation events according to the three

approaches, summed up over the whole period of ten years. PCT: Upper percentile

of N25; DGR: Diameter growth; MEV: Multiple size events.

Center: Average seasonal distribution of particle composition in nmolm^{-3}.

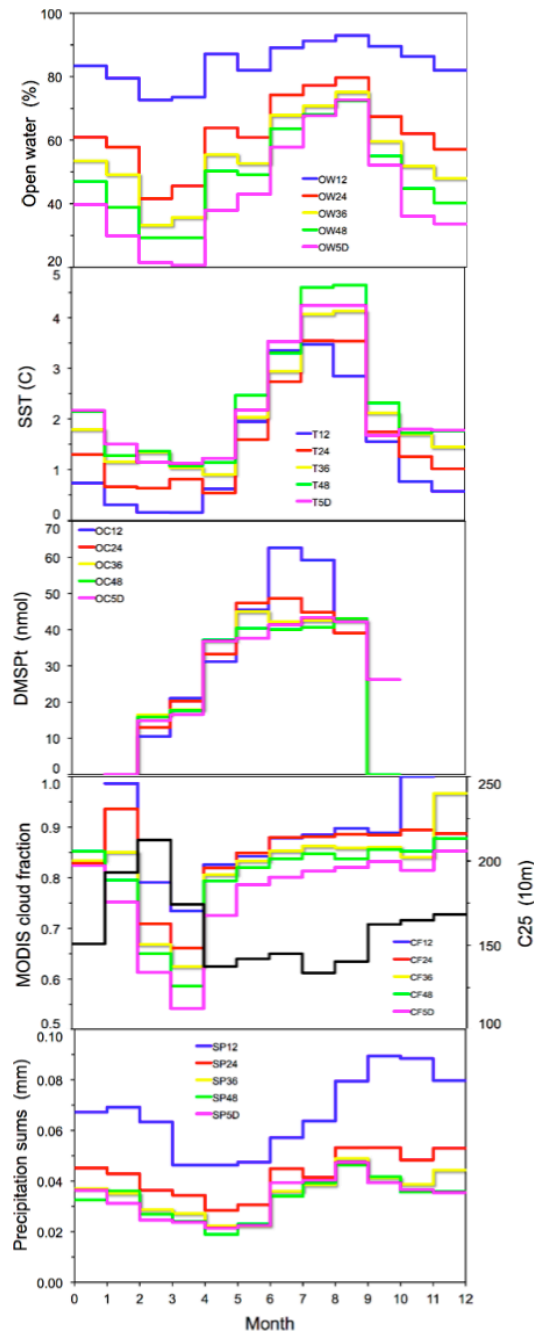Na = sodium, nssSO4 = nssSO$_4^{2-}$, MSA = Methane sulfonate times 100.

Bottom: Monthly average solar flux (SFL, red, Wm^{-2}), and temperature (TEM, blue

°C), and condensation sink, (CS, 10^{5}s^{-1}), at Mt. Zeppelin, Spitsbergen.

1309

1310

1311

1312   Fig. 7   Monthly averages of environmental parameters averaged along back trajectories to

1313   Mt. Zeppelin. From top to bottom: OW12-5D: Open water in % during last 12, 24,

1314   36, and 48h, and days 3-5 before trajectory arrival at Mt. Zeppelin. T12-5D: Same

1315   for sea surface temperature in °C. OC12-5D: Same for DMSPt in nmol in surface

1316   waters.   CF12-5D: Same for MODIS cloud fraction.   SP12-5D: Same for

1317   precipitation sums in mm. C25 = 25%-percentile of cloud base in decameter.

1318
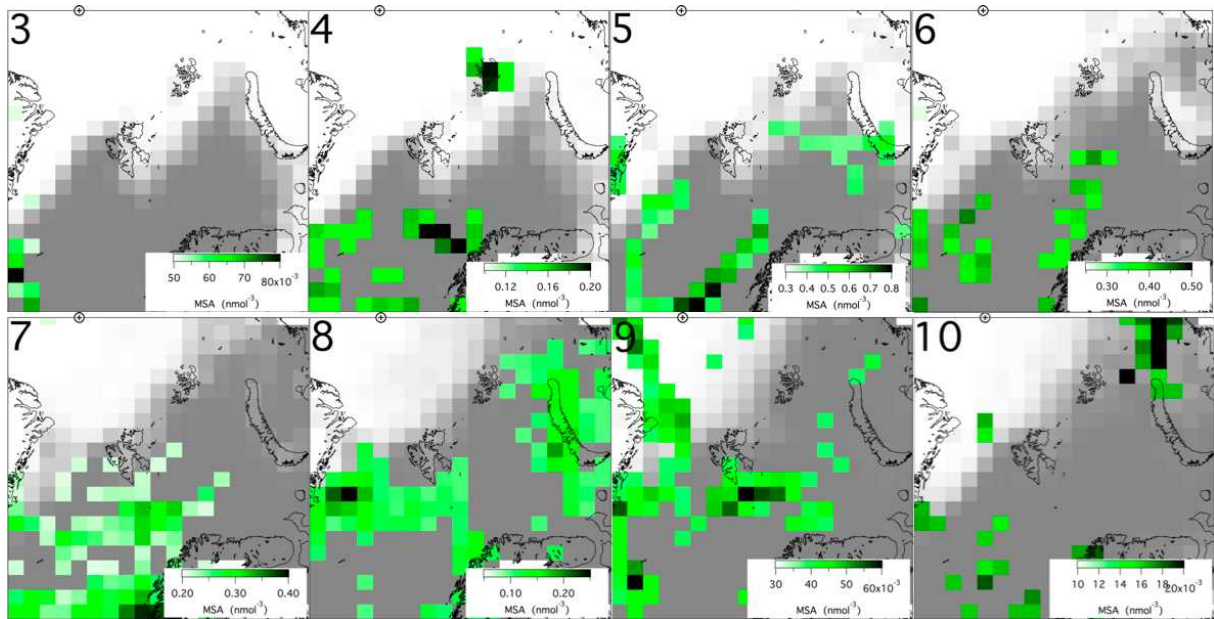
Fig. 8   Average monthly distribution of methane sulfonic acid, (MSA, nmolm^{-3}), during the months March – October of the years 2006 – 2015, constructed from MSA-concentrations measured on Mt. Zeppelin, which were extrapolated along 5-day back trajectories. Average open water percentages during the respective months are indicated as white (0% open water) to dark grey (100% open water) areas. The position of the North Pole is marked as cross in circle on the upper border of the maps.
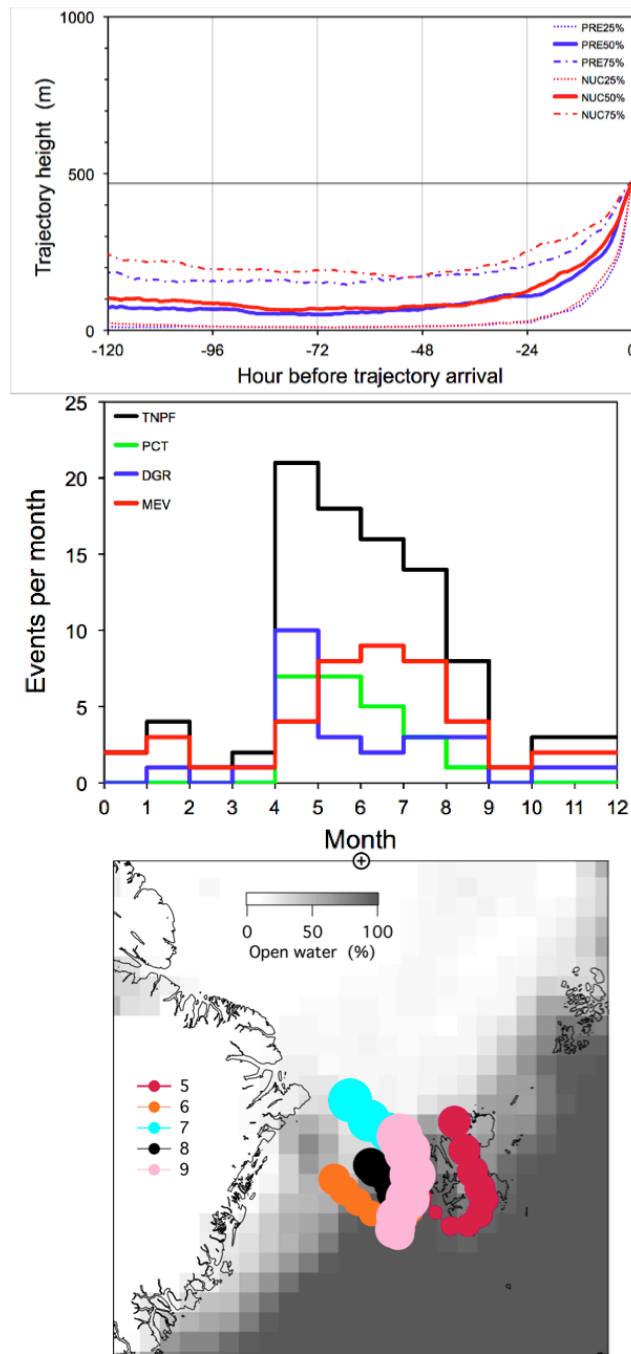
1328

Fig. 9   Characteristics of the subpopulation of 93 NPF-events with back trajectories that
stayed below 500 m for five days before arrival. Top: Statistics of related vertical
trajectory coordinates as in Fig. 5. Center: Average monthly occurrence of PCT,
DGR, and MEV-events, summed up over the whole period of ten years. Bottom:
Related average monthly trajectory positions in 12 h steps for the months May
through September. The circles comprise 95% of all trajectories at any trajectory
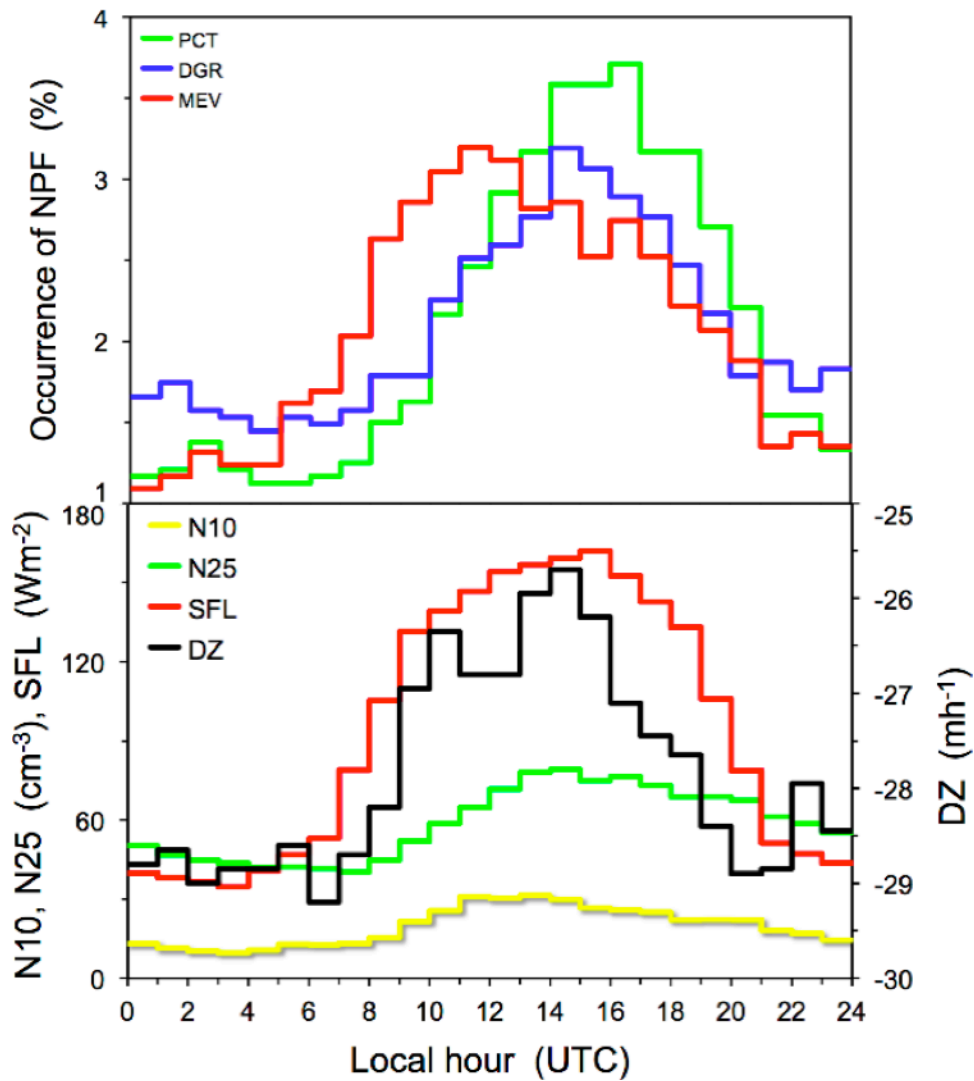
1335   step. The underlying grey-scale map indicates July ice cover averaged over 2006 –

1336   2015.

1337
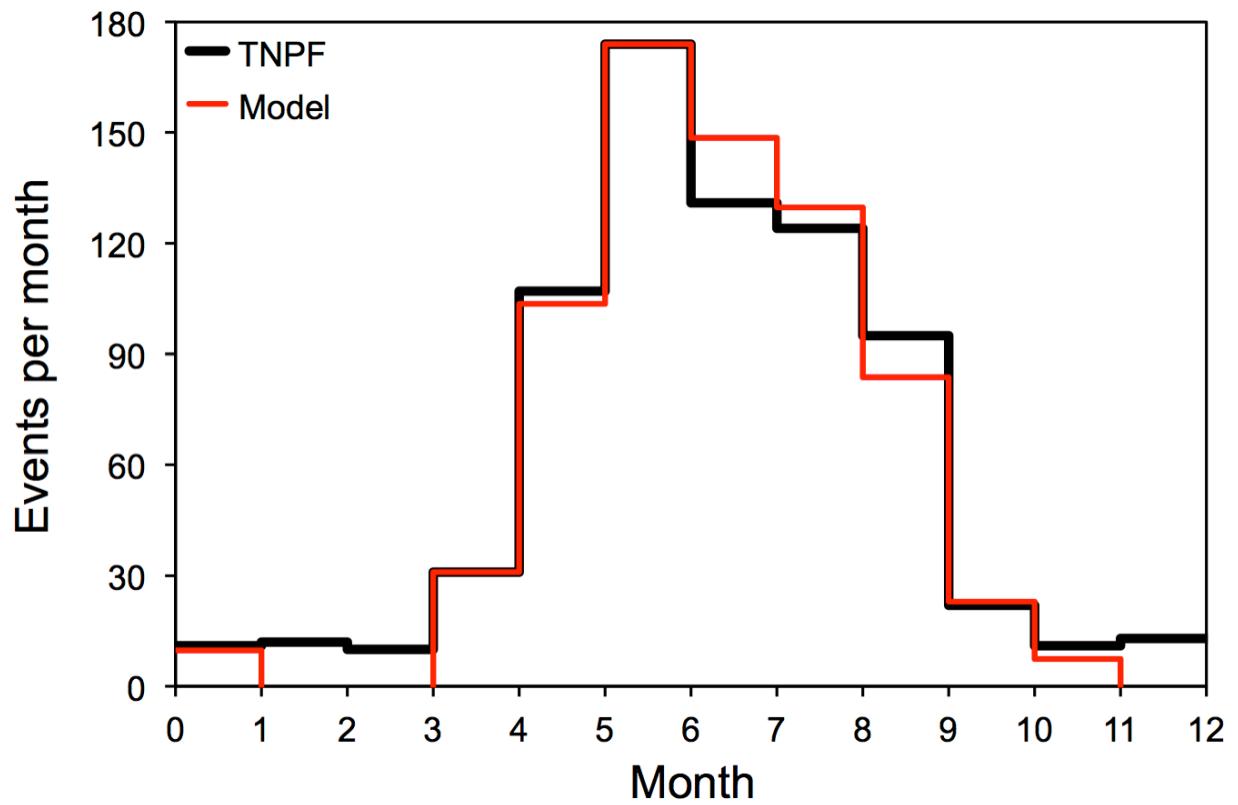
1338

1339   Fig. 10   Average monthly sums of NPF-events due to the three types of new particle

1340   formation, (TNPF, black), summed up over the whole period of ten years.   Red:

1341   Three-parameter model to describe TNPF.

1342

1343

1344 Fig. 11 Top: Relative average diurnal occurrence of the three types NPF-events. PCT:

1345   Upper percentile of N25; DGR: Diameter growth; MEV: Multiple size events.

1346   Bottom: Average diurnal variation of the HYSPLIT-modeled solar flux (SFL, Wm^{-2}),

1347   the integral particle concentrations N10, and N25 in cm^{-3}, and of the vertical

1348   displacement parameter (DZ, mh^{-1}). N10 is based on data of the years 2011 – 2015

1349   whereas the other parameters are based on data of the years 2006 – 2015.